



저작자표시-비영리-변경금지 2.0 대한민국

이용자는 아래의 조건을 따르는 경우에 한하여 자유롭게

- 이 저작물을 복제, 배포, 전송, 전시, 공연 및 방송할 수 있습니다.

다음과 같은 조건을 따라야 합니다:



저작자표시. 귀하는 원저작자를 표시하여야 합니다.



비영리. 귀하는 이 저작물을 영리 목적으로 이용할 수 없습니다.



변경금지. 귀하는 이 저작물을 개작, 변형 또는 가공할 수 없습니다.

- 귀하는, 이 저작물의 재이용이나 배포의 경우, 이 저작물에 적용된 이용허락조건을 명확하게 나타내어야 합니다.
- 저작권자로부터 별도의 허가를 받으면 이러한 조건들은 적용되지 않습니다.

저작권법에 따른 이용자의 권리는 위의 내용에 의하여 영향을 받지 않습니다.

이것은 [이용허락규약\(Legal Code\)](#)을 이해하기 쉽게 요약한 것입니다.

[Disclaimer](#)

공학박사 학위논문

Polymer Designs for High- Performance Anodes in Lithium-Ion and Lithium-Metal Batteries

리튬 이온 및 리튬 메탈 배터리의
고성능 음극을 위한 고분자 디자인

2023 년 2 월

서울대학교 대학원

화학생물공학부

박 기 호

Polymer Designs for High-Performance Anodes in Lithium-Ion and Lithium-Metal Batteries

고성능 리튬 이온, 리튬 메탈 배터리를 위한
고분자 소재 디자인 연구

지도교수 최 장 욱

이 논문을 공학박사 학위논문으로 제출함

2023 년 1 월

서울대학교 대학원
화학생명공학부
박 기 호

박기호의 박사학위논문을 인준함
2023 년 1 월

위 원 장	이 규 태	(인)
부 위 원 장	최 장 욱	(인)
위 원	남 재 욱	(인)
위 원	김 기 재	(인)
위 원	문 준 영	(인)

Abstract

Polymer Designs for High-Performance Anodes in Lithium-Ion and Lithium-Metal Batteries

Kiho Park

School of Chemical & Biological Engineering

The Graduate School

Seoul National University

The advent of lithium ion batteries (LIBs) has brought about a huge change in our lives through the commercialization of electric vehicles (EVs). Although the development of EVs is active and widespread, there is still a need for plans to overcome the issues related to fast charging and long mileage. Therefore, it is important to use materials that can lower the internal resistance and increase the energy density of the batteries. Since the anode active materials have an unstable interface with the electrolyte and changes in structure during the repetitive charging/discharging process, solving such an anode problem is significant. Among various strategies, introducing a polymer into the anode is attracting a lot of attention because it can have a remarkable effect even with a small amount. In this context, we suggest several polymer designs for each anode material including graphite, silicon, and lithium metal, consequently maintaining the interfacial stability and enhancing the electrochemical

performances.

In chapter 1, we report the use of glycerol as an additive to the conventional styrene-butadiene rubber/carboxymethyl cellulose (SBR/CMC) binder for graphite anodes with the aim of lowering the interfacial resistance and thus improving the operating capability at high C-rates. Glycerol, as a plasticizer, increases the interchain free volume in the binder network and also promotes homogeneous charge distribution owing to its high dielectric constant, both of which jointly facilitate lithium ion diffusion at the anode interface. As a result, the addition of a small amount (0.18 wt% of the entire electrode) of glycerol enhances the high-rate capability (i.e., >1C). This study highlights the usefulness of small molecules as binder additives for improving the key performance parameters of LIBs without sacrificing other critical properties.

In chapter 2, we report an elastic binder for silicon/carbon composite electrodes including dynamic Zn^{2+} -imidazole coordination crosslinks and *in situ* crosslinks by thermal treatment during electrode fabrication. The recoverable ability of metal ion-ligand (M-L) coordination bonds and the flexibility of poly(ethylene glycol) chains are unitedly contributive to the superior elasticity of the binder network. This highly elastic binder network integrates particles and then stabilizes the electrode structure, which is consequently responsible for long-term cyclability. As a result of the binder design, stable cycle performance was accomplished in full-cell configuration with commercial levels of areal capacity ($>3 \text{ mAh cm}^{-2}$). The current study highlights the significance of highly reversible Zn (II)-imidazole coordination chemistries for binders intended for high capacity alloying-based electrodes.

In chapter 3, we report a multi-functioning separator combined with fluorinated graphene oxide (**GO-F**) as an inorganic component and polyacrylic acid (PAA)-based polymer as an organic part, which synergistically incorporated to have beneficial components and properties of the SEI layer. By

crosslinking the two materials *via* poly(ethylene glycol) diglycidyl ether (PEGDGE), a robust network of the coating layer on the separator (**OICNS**) was developed. Both the high mechanical strength of **GO-F** and the viscoelastic property of PAA contribute to maintaining the stabilized interface without dendritic Li growth. Especially, the F-functional groups in **GO-F** induce F-enriched inner SEI preemptively, enabling stable electrochemical cycling from the beginning. The current study underlines the importance of a synergistic design of inorganic/organic-composite coated separator in lithium metal batteries (LMBs) through modifying chemical and mechanical properties to form a properly functioning SEI for the highly reversible interface of LMBs.

Keywords : Li-ion battery, Li-Metal battery, Binder Additive, Polymeric binder, Coating layer, Interphase stability

Student Number : 2019-21638

Contents

Chapter 1. Glycerol Additive for Low Resistive Graphite Anodes for Lithium-Ion Batteries	1
1.1 Introduction.....	1
1.2 Experimental section.....	3
1.3 Results and discussion	6
1.4 Conclusion	13
1.5 References.....	13
 Chapter 2. Elastic Zn^{2+} -Imidazole Coordination Binder Network for Silicon Anodes.....	25
2.1 Introduction.....	25
2.2 Experimental section.....	28
2.3 Result and discussion.....	32
2.4 Conclusion	41
2.5 References.....	42
 Chapter 3. Multi-Functioning Separator for High-Performance Lithium-Metal Batteries.....	67
3.1 Introduction.....	67
3.2 Experimental section.....	69
3.3 Result and discussion.....	72
3.4 Conclusion	78
3.5 References.....	79

국문초록	95
------------	----

List of Publications	97
----------------------------	----

List of Figures

Figure 1.1. Graphical illustration of graphite anodes with the (a) SBR/CMC and (b) SBR/CMC+Gly binders.....	18
Figure 1.2. Chemical structures of (a) CMC and (b) glycerol.....	18
Figure 1.3. FT-IR spectra of (a) CMC and glycerol, and (b) the CMC+Gly films with different glycerol contents.....	19
Figure 1.4. (a) Thermogravimetric analysis (TGA) curves of the CMC and CMC+Gly films with different concentrations of glycerol. (b) Differential scanning calorimetry (DSC) profiles of the CMC and CMC+Gly films.....	19
Figure 1.5. Variation in the dielectric constants of the CMC and CMC+Gly films as a function of the frequency	20
Figure 1.6. EIS plots for estimating the Li ion conductivity of polymeric membranes in the (a) Li symmetric and (b) SUS symmetric cells.....	20
Figure 1.7. (a) Viscosity curves of the SBR/CMC and SBR/CMC+Gly slurries at various shear rates. (b) Results of the 180° peeling test of the SBR/CMC and SBR/CMC+Gly electrodes. Graphite loading = 8.1 mg cm ⁻²	21
Figure 1.8. Phase stability test for the SBR/CMC and SBR/CMC+Gly slurries. (a) Photographs of the slurries (a) immediately after preparation and (b) after 3 days	21
Figure 1.9. (a) Photograph of a mixture of glycerol and electrolyte after 3 days. (b) Photograph of the extracted electrolyte after immersing the CMC+Gly (1/1 weight ratio) film in the electrolyte for 3 days. An excess amount of glycerol was introduced to the CMC+Gly film to enable the phase separation to be clearly observed	22
Figure 1.10. CV profiles of CMC and CMC+Gly at the 1st and 15th cycle with Super P (1:1 wt%) at 0.1 mV s ⁻¹ . The CV results in the potential range of (a) 0.01–1.5 V (vs. Li/Li ⁺) and (b) 2.7–4.3 V (vs. Li/Li ⁺)	22

Figure 1.11. Electrochemical results of half-cells based on the SBR/CMC and SBR/CMC+Gly electrodes. (a) Rate capability at various C-rates and (b) corresponding galvanostatic charge-discharge profiles at 0.1C and 2C.....	23
Figure 1.12. Half-cell rate capability of the SBR/CMC electrode and SBR/CMC+Gly electrodes with various glycerol contents to optimize the glycerol amount.....	23
Figure 1.13. Rate capability results of the full-cells in which NCM622 cathodes are paired with graphite anodes containing SBR/CMC and SBR/CMC+Gly.	24
Figure 1.14. Initial profile of NCM622 in the half-cell configuration when scanned at 0.1C (1C = 170.4 mA g ⁻¹)	24
Figure 1.15. EIS profiles of the SBR/CMC and SBR/CMC+Gly electrodes after 5 cycles at 0.5C. Corresponding RSEI and RCT values (right).....	25
Figure 1.16. (a) Equivalent circuit for the EIS measurement. (b) EIS profiles of the SBR/CMC and SBR/CMC+Gly electrodes with different contents of glycerol.....	35
Figure 2.1. (a) Synthetic scheme for the preparation of the metal-ligand complex PEGDGE-Im-Zn²⁺ . (b) Graphical illustration of the supramolecular network on the Si/C composite formed by in situ crosslinking between CMC and PEGDGE-Im-Zn²⁺	49
Figure 2.2. Scheme of the chemical reaction between the hydroxyl and carboxylate groups of CMC and the epoxy group of PEGDGE-Im	50
Figure 2.3. (a) ¹ H NMR spectrum of PEGDGE-Im (DMSO- <i>d</i> ₆ , 400 MHz). (b) Digital photographs of (left) PEGDGE-Im and (right) PEGDGE-Im-Zn²⁺ . (c) Differential scanning calorimetry (DSC) profiles and (d) Raman spectra of PEGDGE-Im and PEGDGE-Im-Zn²⁺ . (e) Solubility test of CMC+(PEGDGE-Im-Zn²⁺) in water before (left) and after (right) in situ crosslinking. (f) Results of the 180° peeling test of the Si/C electrodes with different binders	51

Figure 2.4. (a) FT-IR profiles of PEGDGE and PEGDGE-Im . (b) ^1H NMR spectrum of PEGDGE-Im	52
Figure 2.5. Molecular weight distribution and mean value of PEGDGE-Im	52
Figure 2.6. Raman spectra showing (a) PEG and imidazole in PEGDGE-Im and PEGDGE-Im-Zn²⁺ and (b) imidazole and imidazole-Zn ²⁺ in water	53
Figure 2.7. SEM image and corresponding elemental mapping of PEGDGE-Im-Zn²⁺ using EDS.....	54
Figure 2.8. Raman spectra of (a) PEGDGE-Im and PEGDGE-Im-Zn²⁺ and (b) CMC-PEG-Im and CMC-PEG-Im-Zn²⁺	55
Figure 2.9. Nanoindentation results of CMC-PEG-Im-Zn²⁺ (blue) and CMC (red). Load-displacement curves of the (a) CMC-PEG-Im-Zn²⁺ and (b) CMC films during a loading-unloading cycle. Maximum penetration depths and recovered lengths are denoted along the x-axes. Load-displacement curves of the (c) CMC-PEG-Im-Zn²⁺ and (d) CMC films during the same loading-unloading cycle with plastic work (P) and elastic work (E) noted as areas underneath the curves.....	56
Figure 2.10. Electrochemical test results of half-cells using SBR/CMC, SBR/ CMC-PEG-Im-Zn²⁺ , and PVDF binders. (a) CV profiles of CMC-PEG-Im-Zn²⁺ with Super P (1:1 wt%) at 0.05 mV s ⁻¹ in the potential range of 0.01–1.5 V vs. Li/Li ⁺ . (b) Cycling performance of Si/C electrodes using PVDF (green), SBR/CMC (red), and SBR/ CMC-PEG-Im-Zn²⁺ (blue) measured at 0.5C. (c) Corresponding Coulombic efficiencies in the cycle range of 1–50. (d) Rate capability at various C-rates. (e) Long-term cycling performance of the Si/C electrode containing SBR/ CMC-PEG-Im-Zn²⁺ binder when measured at 0.5C (1.17 mA cm ⁻²).	57
Figure 2.11. XPS results of the CMC-PEG-Im-Zn²⁺ film after 30 CV cycles at 0.5 mV s ⁻¹ in the voltage range of 0.01–1.5 V	58
Figure 2.12. FT-IR spectra of the CMC-PEG-Im-Zn²⁺ film before and after	

30 CV cycles at 0.5 mV s^{-1} in the voltage range of 0.01–1.5 V	58
Figure 2.13. CV profiles of CMC, CMC-PEG-Im-Zn²⁺ with Super P (1:1 wt%), and bare Cu foil at the (a) 1 st cycle, (b) 10 th cycle, and (c) 35 th cycle...	59
Figure 2.14. Cycling performance of the Si/C electrodes containing SBR/CMC-PEG-Im and SBR/CMC-PEG-Im-Zn ²⁺	60
Figure 2.15. Coulombic efficiencies of the Si/C electrodes containing PVDF (green), SBR/CMC (red), SBR/CMC-PEG-Im (gray), and SBR/CMC-PEG-Im-Zn ²⁺ (blue) in the cycle range of 125–200.....	60
Figure 2.16. (a) EIS fitting of electrodes after 10 cycles at 0.5C. (b) Equivalent circuit for the EIS and corresponding resistance results obtained by fitting to the circuit.....	61
Figure 2.17. (a) SEM image and (b) XRD pattern of NCA powder. (c) 1 st charge-discharge profile of NCA under the half-cell configuration when scanned at 0.1C	62
Figure 2.18. Electrochemical performance of the full-cell containing the Si/C electrode with SBR/CMC-PEG-Im-Zn ²⁺ binder. (a) Initial charge-discharge profiles of Si/C-LiNi _{0.8} Co _{0.15} Al _{0.05} O ₂ (NCA) full-cells with different NCA loadings at 0.1C. Cycling performance of the full-cells at 0.5C along with their Coulombic efficiencies over cycling when the NCA loading is (b) 17.18 and (c) 26.83 mg cm ⁻² . The n/p ratios of both cells are 1.1	63
Figure 2.19. Cycling performance of the full-cells based on the SBR/CMC-PEG-Im-Zn ²⁺ , SBR/CMC-PEG-Im, and SBR/CMC binders.....	64
Figure 2.20. Cross-sectional SEM images of Si/C electrodes. (a) Si/C-SBR/CMC electrode after the 30 th delithiation and (b) a magnification of the area within the yellow box. (c) Si/C-SBR/CMC-PEG-Im-Zn ²⁺ electrode after the 30 th delithiation and (d) a magnification of the area enclosed by the yellow box. (e) Thickness changes of the Si/C electrodes after the 30 th delithiation..	65
Figure 2.21. Cross-sectional SEM images of the (a) Si/C-SBR/CMC and (b)	

Si/C-SBR/CMC-PEG-Im-Zn ²⁺ electrodes in the pristine state. The thicknesses of both electrodes were 38 μm	66
Figure 2.22. Cross-sectional SEM images of the (a) Si/C-SBR/CMC and (b) Si/C-SBR/CMC-PEG-Im-Zn ²⁺ electrodes after the 135 th delithiation	66
Figure 2.23. (a) Proposed operating mechanisms of the binders in the electrodes during lithiation and delithiation. (b and c) Photographs of the CMC-PEG-Im-Zn ²⁺ and CMC films before (left) and after (right) two times of bending-unbending action	67
Figure 3.1. Schematic illustrations of Li deposition on Li metal anodes with different separators. (a) Dendritic Li growth is ceaselessly propagated when the pristine poly(propylene) (PP) separator is solely adopted on the Li metal. (b) Uniform Li ion deposition is effectively achieved by using the OICNS between the PP separator and Li metal	83
Figure 3.2. XRD results of GO-F, GO, and graphite	84
Figure 3.3. FT-IR spectra of GO and GO-F	84
Figure 3.4. F 1s XPS spectra of GO-F	85
Figure 3.5. (a) XPS profile of GO and GO-F. (b) High resolution F 1s XPS profile of GO and GO-F	85
Figure 3.6. FT-IR spectra of PAA and LiPAA	86
Figure 3.7. ¹ H NMR spectrum of PAA-PEGDGE (D ₂ O, 400 MHz)	86
Figure 3.8. FT-IR profiles of LiPAA, PEGDGE, and PAA-PEGDGE	87
Figure 3.9. DSC profiles of PAA and PAA-PEGDGE	87
Figure 3.10. TGA curves of PAA and PAA-PEGDGE	88
Figure 3.11. Photographs of (a) PAA+GO-F mixture and (b) the GO-F particles on the PP separator	88
Figure 3.12. Photograph and SEM-EDS elemental mapping of the OICNS	89
Figure 3.13. (a) Electrochemical performances of Li symmetric cells with the PP separator and the OICNS at 1 mA cm ⁻² with a capacity of 1 mAh cm ⁻² . The	

magnified voltage-time curves of Li symmetric cell with the OICNS at 1 mA cm ⁻² with a capacity of 1 mAh cm ⁻² (b) from 600 h to 606 h and (c) from 994 h to 1000 h.....	89
Figure 3.14. Electrochemical performances of Li symmetric cell with PAA+ GO-F layer at 1 mA cm ⁻² with a capacity of 1 mAh cm ⁻²	90
Figure 3.15. The EIS spectra of Li symmetric cells with (a) the PP separator and (b) the OICNS after 1 st , 5 th , 20 th , and 50 th cycle.....	90
Figure 3.16. F 1s XPS depth profiles of Li metal anodes after 5 cycles for (a) the PP separator and (b) the OICNS	91
Figure 3.17. Electrochemical performance of LFP-Li full-cells with the PP separator and the OICNS . Cycling performance of the full cells at 0.5C when the mass loading of LFP is (a) 10.0 mg cm ⁻² and (b) their coulombic efficiencies. (c) Rate performance of LFP-Li full cells containing the PP separator and the OICNS	92
Figure 3.18. Cross-sectional SEM images of Li metal electrodes after 20 th discharge with (a) the PP separator and (b) the OICNS	93
Figure 3.19. (a) SEM images of Li metal electrodes after 20 th cycling in Li symmetric cells with the PP separator and (b) magnification of the area enclosed by the white box.	94
Figure 3.20. SEM images of Li metal electrodes after 20 th cycling in Li symmetric cells with the OICNS	94

Chapter 1. Glycerol Additive for Low Resistive Graphite Anodes for Lithium-Ion Batteries

1.1 Introduction

Efficient energy storage is a key element for building a complete, sustainable energy cycle, and one of the most remarkable state-of-the-art technologies along this direction is lithium-ion batteries (LIBs). LIBs have successfully been used to power a variety of mobile electronic devices and eco-friendly electric vehicles (EVs).^[1] Although LIBs have continuously evolved in various respects, their application, particularly in the vehicle sector, has had to meet ever-challenging goals in terms of their key metrics including their energy density, power density, lifetime, and safety. Progress in LIB technology appears to have been mainly driven by the discovery of active materials. With respect to the anode, graphite has been the dominant material for the past decades owing to its high (electro)chemical stability in the low-potential regime, natural abundance, and low cost. Currently, the graphite content of practical cells still accounts for more than 90 wt% of the anode components even if the community was to pursue the incorporation of other materials with high specific capacities such as silicon. In spite of the remarkable dominance of LIBs in commercial products, various factors contributing to the performance of graphite anodes still need to be improved. Among these factors, high-power and fast charging capability has become highly urgent.

The high-power and fast charging operation of the graphite anode is affected by multiple parameters as the lithium (Li) ion diffusion can be impeded by various electrode components. Particularly, Li ions need to overcome the

energy barriers they encounter when traversing the solid-electrolyte-interphase (SEI) layer and the inter-particle space surrounded by the conductive agent and polymeric binder as well as those that exist along the diffusion paths in the interlayer space in the graphite.^[2] The effect of the diffusion barriers is exacerbated at high C-rates and in highly loaded electrodes. Importantly, the inter-diffusional resistance within the graphite lattice is much lower than the interfacial resistance offered by the SEI layer and inter-particle space.^[3] This is the main rationale behind the observation that the electrolyte composition and choice of binder have a substantial effect on the high-rate performance.^[4] From the viewpoint of electrolyte engineering, in particular, various additives were identified to lower the SEI resistance of the electrodes.^[5] A photochemical approach that induces an inorganic-rich SEI composition was also found to be favorable for high C-rate operation.^[6] Another approach involved the magnetic alignment of graphite to induce directional Li ion diffusion with minimal tortuosity and thus support high-rate cycling.^[2b] The binder would also be expected to play a crucial role in decreasing the resistance for Li ion diffusion.^[7] One clear direction in this vein would entail lowering the binder content of the electrode, but the binder content of present commercial LIB cells does not leave much room to this end. More challenging is that structural modifications of widely adopted binders may not be a viable option because they could perturb other favorable properties such as the slurry viscosity and adhesion to active particles.

Small molecules have been widely adopted as plasticizers in polymer engineering to lubricate the backbones of the mother polymer.^[8] Upon introduction, the plasticizers penetrate the network of polymer chains and increase the chain flexibility. As a result, the collective polymeric motion lowers the glass transition temperature (T_g).^[9] Benchmarking the approach of adopting plasticizers consisting of small molecules, we anticipated that the

motions of the polymeric chains of the binder could also be increased to facilitate Li ion diffusion within the binder network. This prompted us to introduce glycerol to graphite anodes based on the conventional styrene-butadiene rubber/carboxymethyl cellulose (SBR/CMC) binder as a binder additive. SBR/CMC blends are currently the most popular binders for the anodes in LIBs owing to their excellent water solubility, good stability in the potential range in which anodes are operated as well as the cooperative functioning of their individual components.^[10] Specifically, SBR functions as a cushion to buffer the stress caused by the volume change of active particles, whereas CMC is highly amicable to the graphite surface bridges between the graphite and SBR. CMC also serves to thicken the slurry and thus contributes to improving the adhesion of the coating to the electrode. However, the SBR/CMC blend does not largely support Li ion conduction; instead,^[11] it increases the resistance of the electrode film considerably^[12] (Figure 1.1a). Contrary to this, as illustrated in Figure 1.1b, the glycerol additive can easily and deeply penetrate the CMC network^[13] to increase its interchain free volume. This increase in the free volume enhances the chain mobility and consequently lowers the crystallinity of the polymer collectively.^[14] Apart from this, the high dielectric constant of glycerol promotes the dissociation of Li salt and thus further increases the Li ion conductivity of the electrode.^[15] Our study demonstrates that the integration of a small-molecule additive improves the key battery performance parameters without sacrificing the properties of the original mother binder in both the slurry and electrode states, and could thus be widely adopted for various types of electrodes in practical cells.

1.2 Experimental section

Materials and chemicals. Na-CMC, SBR, poly(vinylidene fluoride) (PVdF), and glycerol were purchased from Sigma-Aldrich (USA). $\text{LiNi}_{0.6}\text{Co}_{0.2}\text{Mn}_{0.2}\text{O}_2$ (NCM622) was purchased from LANDF Co. (South Korea). Super P was purchased from Timcal (Switzerland). *N*-methyl-2-pyrrolidone (NMP) solvent was purchased from Junsei (Japan). Graphite, 1.0 M lithium hexafluorophosphate (LiPF_6) in ethylene carbonate (EC)/diethylene carbonate (DEC) (1/1 volume ratio) containing 10 wt% fluoroethylene carbonate (FEC), and polyethylene (PE) film were purchased from Welcos (South Korea).

Characterization. Fourier transform-infrared spectroscopy (FT-IR) (SENSOR27, Bruker) and thermogravimetric analysis (TGA) (TA Instruments, Discovery TGA) were used to prove the presence of glycerol in the CMC film. The TGA was conducted under nitrogen (N_2) atmosphere in the range 30–550 °C at a ramping rate of 10 °C min^{-1} . The glass transition temperature (T_g) was measured using differential scanning calorimetry (DSC) (PerkinElmer DSC 4000) at a ramping rate of 10 °C min^{-1} . The permittivity was obtained using an LCR Meter (Agilent) with the ASTM D150 method ranging from 0.1 MHz to 13 MHz. To evaluate the ionic conductivity, glass fiber membranes that were 16 mm in diameter were dipped in the CMC and CMC/glycerol (CMC+Gly) solutions based on deionized water and were then dried at 70 °C for 3 days. Next, 10 μL of electrolyte comprising 1.0 M LiPF_6 in EC/ DEC (1/1 volume ratio) including 10 wt% FEC was dropped onto the polymer-coated glass fiber membranes, followed by assembly into CR2032 type coin cells with a symmetric Li or steel-use-stainless (SUS) electrode configuration. The electrochemical impedance spectroscopy (EIS) tests were then performed using a potentiostat (VSP, Biologic) in the frequency range from 1 MHz to 0.1 Hz.

The viscosity of the slurries was measured using a stress-controlled rheometer with a 40 mm flat plate (Discovery HR-2, TA Instruments). For these measurements, the temperature was kept at 25 °C. The 180° peeling adhesion tests were conducted using a universal testing machine (UTM) (QM100s, QMESYS). For the characterizations except for FT-IR and TGA, the CMC+Gly films were prepared by adding 20 wt% of glycerol with respect to CMC.

Preparation of electrodes. The slurry was prepared by dispersing the graphite and SBR/CMC binder in deionized water in a weight ratio of 98:2. The weight ratio between SBR and CMC was 1:1. The electrode to which glycerol had been added (SBR/CMC+Gly) was fabricated by injecting various amounts (10–30 wt%) of glycerol with respect to CMC. The slurries were cast on copper foil using the doctor blading method. The electrodes were fully dried at 100 °C for 10 min, followed by additional drying at 60 °C under vacuum overnight. The electrodes were then compressed using a roll-pressor to achieve the loading density of 1.4 g cm⁻³. The mass loading of active material was 8.1 mg cm⁻². The cathodes for full-cell tests were fabricated to contain NCM622, PVdF, and Super P in a weight ratio of 90:5:5. The slurry for these cathodes was based on NMP. The slurry was cast on aluminum foil and underwent drying at 60 °C under vacuum overnight.

Electrochemical measurement. All electrochemical tests were conducted using CR2032 type coin cells assembled in an argon-filled glove box. In both the half-cell and full-cell tests, the diameter of the electrodes was 10 mm. The electrolyte was 1.0 M LiPF₆ in EC/DEC (1/1 volume ratio) containing 10 wt% FEC. PE film was used as a separator. A battery cycler (WBCS 3000,

WonATech) was operated at 25 °C to record all the electrochemical results. For half-cell tests, one pre-cycle was run at 0.1C to form a stable SEI, after which subsequent cycling was conducted at 0.5C in constant current (CC) mode in the potential range of 0.01–1.5 V (*vs.* Li/Li⁺) except for the rate capability tests. The full-cell tests were carried out with one pre-cycle at 0.1C and subsequent cycles at 0.5C in the potential range of 2.7–4.3 V in CC mode. The n/p ratio was set to 1.1, and the NCM622 loading was 15.2 mg cm⁻². For the rate capability tests, both half- and full-cells were scanned at various C-rates from 0.1C to 2.0 C. Cyclic voltammetry (CV) tests were performed at a scan rate of 0.1 mV s⁻¹ in the potential range of 0.01–1.5 V (*vs.* Li/Li⁺) for the anode side and 2.7–4.3 V (*vs.* Li/Li⁺) for the cathode side. The EIS tests were conducted using a potentiostat (VSP, Biologic) in the frequency range from 1 MHz to 0.01 Hz.

1.3 Results and discussion

Figure 1.2 presents the chemical structures of CMC and glycerol, and their FT-IR spectra are displayed in Figure 1.3a. The spectrum of CMC exhibited its characteristic peaks at 3274, 2885, 1589, 1413, and 1018 cm⁻¹. The broad band at 3274 cm⁻¹ corresponds to the O–H stretching vibration arising from the formation of strong hydrogen bonds involving the hydroxyl and carboxylate groups of CMC. The band at 1589 cm⁻¹ is associated with the C=O asymmetric vibrations of the carboxylate group. The peak at 2885 cm⁻¹ corresponds to the C–H anti-symmetrical stretching vibration in CMC.^[16] The glycerol is composed of two primary alcohols and one secondary alcohol, as revealed by their respective C–O stretching peaks at 1030 and 1108 cm⁻¹.

Additionally, the broad band at 3285 cm^{-1} is related to the stretching of both the primary and secondary O–H in glycerol.^[9] As for the CMC+Gly combination, the bands originating from the individual components were all observed at 3274 , 2874 , 1594 , 1320 , and 1030 cm^{-1} . (Figure 1.3b) When the glycerol content of the films was increased, the signature peaks of glycerol at 3274 , 1320 , and 1030 cm^{-1} intensified accordingly, verifying that glycerol was well embedded in the CMC matrix.

The TGA curves of the CMC and CMC+Gly films are presented for the temperature range from 30 to $550\text{ }^{\circ}\text{C}$ in Figure 1.4a. For both samples, the weight losses in the range of 30 – $100\text{ }^{\circ}\text{C}$ were related to the evaporation of free water. In the case of bare CMC, one-stage decomposition was observed at around $260\text{ }^{\circ}\text{C}$, which reflects the degradation of the main cellulose skeleton. On the other hand, the CMC+Gly underwent a two-stage weight loss. The first of these stages in the range of 120 – $240\text{ }^{\circ}\text{C}$ corresponds to the degradation of glycerol,^[9] whereas the second stage near $240\text{ }^{\circ}\text{C}$ corresponds to the decomposition of the main chains of CMC. As a proof of this interpretation, an increase in the glycerol content of the CMC matrix gave rise to an increase in the mass loss in the temperature range of 120 – $240\text{ }^{\circ}\text{C}$ owing to the decomposition of the greater amount of glycerol.

The T_g of the polymers was investigated using DSC analysis. The T_g is the temperature at which the glassy state of a polymer is converted to its rubbery state and thus points to a thermophysical transition. Hence, a lower T_g represents a more flexible polymer network based on the higher mobility of the individual chains.^[17] On the basis of this logic, the lowered T_g of the polymer resulting from the addition of a plasticizer can be understood in relation to the enhanced chain motions, which increase the free volume in the interchain space.^[18] Figure 1.4b shows the DSC curves of the CMC and CMC+Gly films,

which reveal that their respective T_g were 109 and 101 °C; as expected, the addition of glycerol as a plasticizer effectively lowered the T_g of the original CMC.

The effect of adding glycerol on the dielectric property was also examined. Figure 1.5 presents plots of the dielectric constant vs. the frequency for the CMC and the CMC+Gly films at room temperature. The dielectric constant of the CMC+Gly film remained higher than that of its CMC film counterpart throughout the entire frequency range from 0.1 MHz to 13 MHz. The higher dielectric constant of the CMC+Gly was contributed by glycerol, which has an inherently high dielectric constant.^[19] The higher dielectric constant would be considered to be useful for enhancing the Li ionic conductivity by facilitating the dissociation of ion pairs inside the polymer network.

To assess the ionic transport at the interface, the polymer membranes with and without glycerol were subjected to EIS analysis (Figure 1.6). We performed these tests in two types of symmetric cells, namely, Li|Li and SUS|SUS cells. In each EIS plot, the diameter of the semi-circle and the x -intercept represent the charge transfer resistance (R_{CT}) and bulk resistance (R_b), respectively, for the Li ion transport through the membrane. In the Li|Li symmetric cells, the R_{CT} for the CMC+Gly and CMC cells was 351.8 and 387.3 Ω , respectively (Figure 1.6a). Following the same trend, their R_b was 56.8 and 88.2 Ω , respectively (Figure 1.6b). Hence, the addition of glycerol indeed lowered the bulk and interfacial resistance of the CMC membrane significantly, supporting the role of glycerol as a plasticizer and emphasizing the usefulness of its high dielectric constant. Although these two functions of glycerol jointly lowered the two forms of resistance, their individual contributions are difficult to separate.

In the actual manufacturing process, the addition of an additive to a slurry is not trivial at all because it could perturb the rheological properties of the original slurry, which could have a negative effect on the physicochemical and electrochemical properties of the electrode to be fabricated.^[20] With this concern in mind, the SBR/CMC+Gly slurry was prepared by adding 20 wt% glycerol with respect to CMC, and its rheological property was compared with those of the SBR/CMC slurry at various shear rates. (Figure 1.7a). Both slurries exhibited almost identical shear-thinning characteristics over the entire range of shear rates of 0.1–1000 s⁻¹, verifying that the addition of glycerol did not alter the intrinsic rheological stability of the SBR/CMC slurry. In a similar context, the long-term stability of the slurry was evaluated by leaving the slurries for 3 days (Figure 1.8). Neither of the slurries underwent any phase separation after 3 days, pointing to the fact that the addition of glycerol did not destabilize the polymeric network in the slurry.

We also examined the electrode adhesion because the addition of glycerol could perturb the established adhesion by SBR/CMC. To this end, 180° peeling tests were conducted using a displacement of 5–15 mm. The adhesion force of the SBR/CMC+Gly electrode was comparable to that of its SBR/CMC counterpart: 0.692 vs. 0.686 gf mm⁻¹ (Figure 1.7b). Similar to the viscosity tests, these results of the peeling tests verified that glycerol did not adversely affect the adhesion property of the electrode. Rather, the slightly improved adhesion of SBR/CMC+Gly might imply that the addition of glycerol compensates for the rigidity of CMC.²¹

Having noted that a small-molecule additive in the electrode could potentially dissolve into the electrolyte, the miscibility between glycerol and the carbonate-based electrolyte was evaluated. Because both the additive and the electrolyte are liquids, in this test, glycerol and EC/DEC (1/1 volume ratio)

were mixed and allowed to rest for 3 days. After this period, the mixture had clearly undergone a phase separation into the two respective liquids (Figure 1.9a). Separately, the CMC+Gly film was soaked in the electrolyte for 3 days, but phase separation was not observed to have occurred at all (Figure 1.9b), indicating that the glycerol firmly remained in the CMC film owing to hydrogen bonding interaction between the hydroxyl functional groups of glycerol and the carboxylate and hydroxyl functional groups of CMC.²²

The electrochemical stability of CMC+Gly was evaluated by carrying out a cyclic voltammetry (CV) test of its polymer film containing Super P in the potential ranges of 0.01–1.5 V and 2.7–4.3 V (vs. Li/Li⁺) (Figure 1.10). Regardless of the presence of glycerol, the CV results of both the CMC+Gly and CMC films were almost identical throughout 15 cycles in both of these potential regimes, implying that glycerol was not decomposed during cycling across the entire potential range for full-cells.

Most importantly, the effect of glycerol on the rate performance was assessed by varying the C-rate from 0.1C to 2C (1C=350 mA g⁻¹) (Figure 1.11a) in the half-cell setting where the areal loading of graphite was 8.1 mg cm⁻². The optimum content of glycerol in the electrode was identified to be 20 wt% with respect to CMC according to rate capability tests that underwent various C-rates while varying the content of glycerol (Figure 1.12). Thus, our discussion hereafter is focused on the electrodes with this content of glycerol. The SBR/CMC+Gly electrode exhibited a charge-discharge profile similar to that of its SBR/CMC counterpart in the pre-cycle at 0.1C (Figure 1.11b), reconfirming that the mechanism of Li storage remained unscathed even after the addition of glycerol. At 0.2C, both the SBR/CMC and SBR/CMC+Gly electrodes had similar specific reversible capacities near 340 mAh g⁻¹. However, as the C-rate was raised, the SBR/CMC+Gly electrode displayed distinctly

higher capacities. Specifically, the SBR/CMC+Gly electrode retained 297.6, 243.3, 185.1, 114.5, and 65.6 mAh g⁻¹ at 0.5C, 0.7C, 1C, 1.5C, and 2C, respectively, whereas the SBR/CMC electrode retained only 285.3, 231.9, 173.6, 106.9, and 59.1 mAh g⁻¹ at the same C-rates. Once again, the observed distinct performance is attributed to glycerol, which enhanced the Li ion conductivity by increasing the mobility of the CMC backbone. In addition, the Li ion conductivity also benefited from the high dielectric constant of glycerol. Although the capacities of the SBR/CMC+Gly electrode stayed higher at all the C-rates, the capacity difference at 1.5C and 2C was not as much as expected. This observation can be explained by the operating conditions during the half-cell measurements; at the high C-rate at which the polarization is enlarged, the potential of the electrode can easily reach the bottom cut-off voltage of 0.01 V (vs. Li/Li⁺) before fully exhibiting the staging effect of graphite by which most of its capacity is delivered (Figure 1.11b). The large polarization is contributed significantly by the Li metal counter electrode.^[6, 23]

To avoid this limitation in the half-cell measurements, the rate capability tests were performed in the full-cell setting by pairing with NCM622 with an areal loading of 15.2 mg cm⁻² (Figure 1.13). The specific capacity of the NCM622 cathode was 170.4 mAh g⁻¹ at 0.1C (Figure 1.14), and the n/p ratio defined by the capacity ratio between the anode and cathode was set to 1.1 by benchmarking the literature.^[24] The SBR/CMC+Gly full-cell showed conspicuously superior capacity retention on increasing the C-rate. Most notably, at 2C, the average capacity of the SBR/CMC+Gly electrode was 106.6 mAh g⁻¹ whereas that of the SBR/CMC electrode was only 75.2 mAh g⁻¹ such that the average capacity of the SBR/CMC+Gly electrode was higher by 41.8%. These capacities at 2C correspond to capacity retentions of 67.9% and 47.3% as compared to those of both electrodes at 0.2C, respectively. Hence, the effect of glycerol was unveiled most drastically at high C-rates in full-cell operation.

Remarkably, given the fact that reliable operation at high C-rates is the most critical requirement for pushing the limit of high-power and supercharging capability, the enlarged capacity gap at 2C indicates that glycerol can play a central role in improving these properties. When the C-rate returned to 0.2C, the capacity of the SBR/CMC+Gly electrode was fully recovered, verifying that glycerol did not impair the original sustainability of the graphite electrode even during harsh operations.

The enhancement of the kinetics of Li storage was confirmed by the EIS results after 5 cycles (Figure 1.15 and Figure 1.16a). The EIS profiles of both cells presented two semi-circles in the high- and medium-frequency regimes, respectively. The first semi-circle in the high-frequency regime represents the SEI resistance (R_{SEI}), which originates from the impedance of the interfacial layer. The second semi-circle in the medium-frequency regime corresponds to the charge transfer resistance (R_{CT}) at the interface.^[25] Based on the Nyquist plots, both R_{SEI} and R_{CT} of the SBR/CMC+Gly electrode were smaller than those of the SBR/CMC electrode. Notably, R_{CT} of the SBR/CMC+Gly electrode was significantly smaller compared with that of the SBR/CMC electrode (37.5 Ω vs. 51.1 Ω), which reflects the improved kinetics of the Li ion transport and intercalation along the interface. In particular, the enhanced charge transfer kinetics resulting from the addition of glycerol is closely associated with facile Li ion migration in the more mobile polymer network as well as the easier dissociation of the ion-pairs as a result of the greater dielectric constant. Consistent with the rate capability results in Figure 1.12, the SBR/CMC+Gly electrode containing 20 wt% of glycerol with respect to CMC exhibited the smallest semi-circles among all with various glycerol contents (Figure 1.16b). All in all, the addition of a small amount of glycerol improved the high-power and fast charging capability markedly, and this enhanced performance mainly stems from the more facile charge transfer at the

interface.

1.4 Conclusions

Improving the high-rate and supercharging capability without sacrificing other key properties is nontrivial even in established LIB technology. The present study highlights the importance of glycerol as a binder additive in that the addition of a small amount of glycerol increases the specific capacity at high C-rates prominently while preserving the original physicochemical and electrochemical properties of the graphite anode. Glycerol, as a plasticizer, broadens the interchain free volume in the polymer network for more facile Li ion migration. The high dielectric constant of glycerol also contributes to promoting Li ion transport by freeing the Li cation from its ion pair with the anion. These features of glycerol were demonstrated to be particularly advantageous for lowering the charge transfer resistance at the interface. The concept of adding glycerol as a small-molecule additive indicates that the knowledge and expertise established in polymer science can be usefully adopted to advance binder technology in LIBs.

1.5 References

- [1] J. B. Goodenough, K.-S. Park, *J. Am. Chem. Soc.*, **2013**, 135, 1167; b) J. W. Choi, D. Aurbach, *Nat. Rev. Mater.* **2016**, 1, 1.
- [2] a) Y. J. Oh, J. H. Park, J. S. Park, S. S. Kim, S. J. Hong, Y. W. Na, J. H. Kim, S. Nam, S. J. Yang, *Energy Storage Mater.* **2021**, 44, 416; b) J. Billaud, F. Bouville, T. Magrini, C. Villevieille, A. R. Studart, *Nat. Energy* **2016**, 1, 1.

- [3] K. Persson, V. A. Sethuraman, L. J. Hardwick, Y. Hinuma, Y. S. Meng, A. van der Ven, V. Srinivasan, R. Kostecki, G. Ceder, *J. Phys. Chem. Lett.* **2011**, *1*, 1176.
- [4] M. Wu, X. Xiao, N. Vukmirovic, S. Xun, P. K. Das, X. Song, P. Olalde-Velasco, D. Wang, A. Z. Weber, L.-W. Wang, V. S. Battaglia, W. Yang, G. Liu, *J. Am. Chem. Soc.* **2013**, *135*, 12048.
- [5] a) Y. Okuno, K. Ushirogata, K. Sodeyama, Y. Tateyama, *Phys. Chem. Chem. Phys.*, **2016**, *18*, 8643; b) Y. Wang, Y. Liu, Y. Tu, Q. Wang, *J. Phys. Chem. C* **2020**, *124*, 9099.
- [6] M. Baek, J. Kim, J. Jin, J. W. Choi, *Nat. Commun.* **2021**, *12*, 1.
- [7] a) J. Kim, J. Lee, J. You, M.-S Park, M. S. A. Hossain, Y. Yamauchi, J. H. Kim, *Mater. Horiz.* **2016**, *3*, 57; b) J. Kim, J. H. Kim, and K. Ariga, *Joule* **2017**, *1*, 739.
- [8] M. Bocqué, C. Voirin, V. Lapinte, S. Caillol, J. J. Robin, *J. Polym. Sci., Part A: Polym. Chem.* **2016**, *54*, 11.
- [9] a) Y. Sun, C. Meng, Y. Zheng, Y. Xie, W. He, Y. Wang, K. Qiao, L. Yue, *Cellulose* **2018**, *25*, 5893; b) S. C. Teixeira, R. R. A. Silva, T. V. de Oliveira, P. C. Stringheta, M. R. M. R. Pinto, N. d. F. F. Soares, *Food Biosci.* **2021**, *42*, 101202.
- [10] a) T.-w. Kwon, J. W. Choi, A. Coskun, *Chem. Soc. Rev.* **2018**, *47*, 2145; b) J. Kim, K. Park, Y. Cho, H. Shin, S. Kim, K. Char, J. W. Choi, *Adv. Sci.* **2021**, *8*, 2004290; c) C. Wei, M. N. Obrovac, *J. Electrochem. Soc.* **2019**, *166*, A3217.
- [11] J.-Y. Eom, L. Cao, *J. Power Sources* **2019**, *441*, 227178.

- [12] J.-P. Yen, C.-C. Chang, Y.-R. Lin, S.-T. Shen, J.-L. Hong, *J. Electrochem. Soc.* **2013**, *160*, A1811.
- [13] D. Marín-Peñalver, A. Alemán, M. C. Gómez-Guillén, P. Montero, *Food Hydrocoll.* **2019**, *94*, 553.
- [14] S. Zekriardehani, S. A. Jabarin, D. R. Gidley, M. R. Coleman, *Macromolecules* **2017**, *50*, 2845.
- [15] a) J. Lopez, D. G. Mackanic, Y. Cui, Z. Bao, *Nat. Rev. Mater.* **2019**, *4*, 312; b) O. Tamwattana, H. Park, J. Kim, I. Hwang, G. Yoon, T.-h. Hwang, Y.-S. Kang, J. Park, N. Meethong, K. Kang, *ACS Energy Lett.* **2021**, *6*, 4416.
- [16] B. Kumar, F. Deebea, R. Priyadarshi, Sauraj, S. Bano, A. Kumar, Y. S. Negi, *Polym. Bull.* **2020**, *77*, 4555.
- [17] J. Zhang, Z. Huang, D. Liu, *Appl. Surf. Sci.* **2017**, *426*, 796.
- [18] M. G. A. Vieira, M. A. da Silva, L. O. dos Santos, M. M. Beppu, *Eur. Polym. J.* **2011**, *47*, 254.
- [19] P. Mazurek, L. Yu, R. Gerhard, W. Wirges, A. L. Skov, *J. Appl. Polym. Sci.* **2016**, *133*, 44153.
- [20] a) B. Bitsch, J. Dittmann, M. Schmitt, P. Scharfer, W. Schabel, N. Willenbacher, *J. Power Sources* **2014**, *265*, 81; b) D. Y. Kim, K. H. Ahn, *Nihon Reoroji Gakkaishi* **2021**, *49*, 127.
- [21] J. S. Behra, J. Mattsson, O. J. Cayre, E. S. J. Robles, H. Tang, T. N. Hunter, *ACS Appl. Polym. Mater.* **2019**, *1*, 344.
- [22] M. Esmacili, G. Pircheraghi, and R. Bagheri, *Polym. Int.* **2017**, *66*, 809.
- [23] T. Ohzuku, Y. Iwakoshi, K. Sawai, *J. Electrochem. Soc.* **1993**, *140*,

2490.

[24] S. J. An, J. Li, C. Daniel, D. Mohanty, S. Nagpure, D. L. Wood III, *Carbon* **2016**, *105*, 52.

[25] W. Choi, H.-C. Shin, J. M. Kim, J.-Y. Choi, W.-S. Yoon, *J. Electrochem. Sci. Technol.* **2020**, *11*, 1.

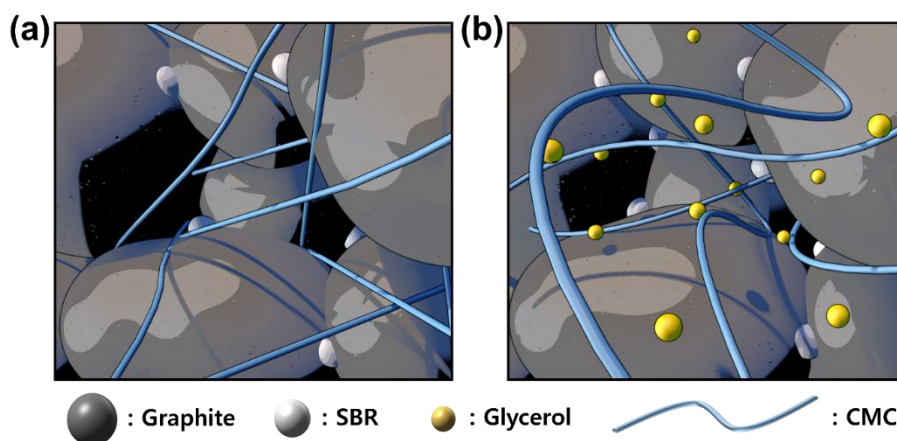


Figure 1.1. Graphical illustration of graphite anodes with the (a) SBR/CMC and (b) SBR/CMC+Gly binders.

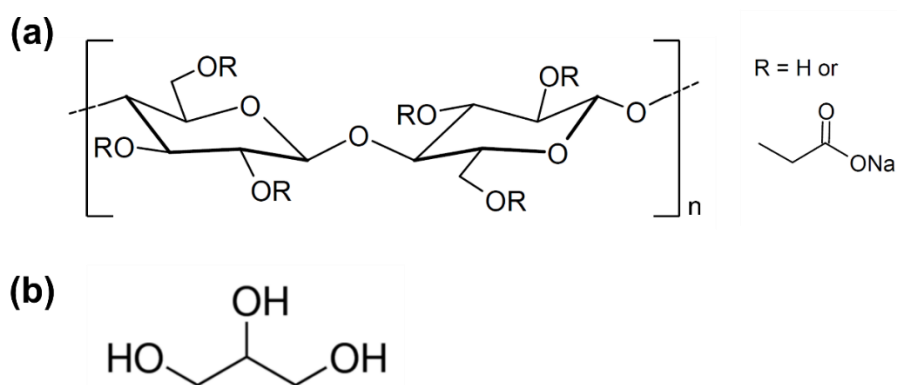


Figure 1.2. Chemical structures of (a) CMC and (b) glycerol.

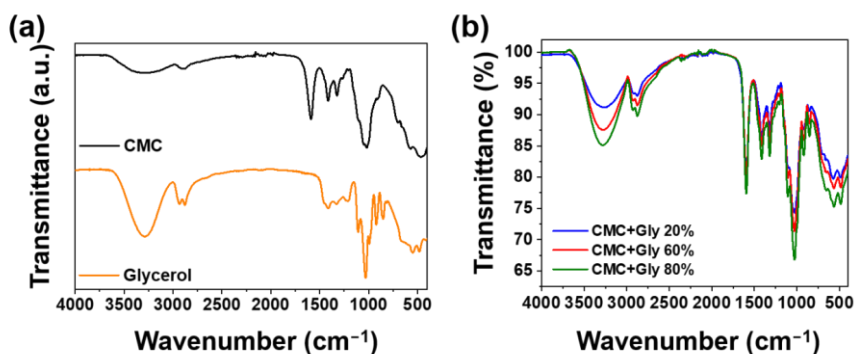


Figure 1.3. FT-IR spectra of (a) CMC and glycerol, and (b) the CMC+Gly films with different glycerol contents.

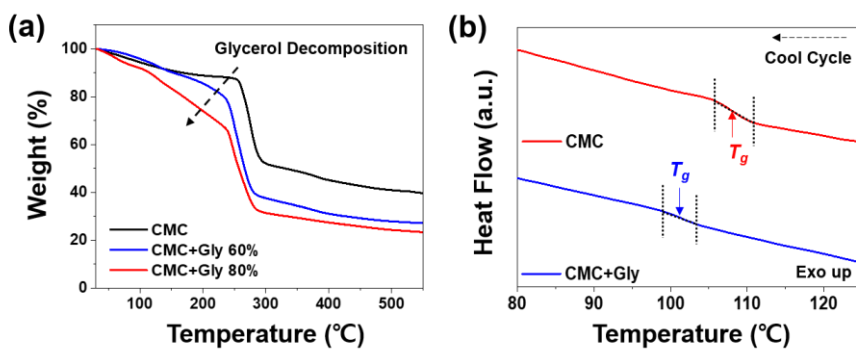


Figure 1.4. (a) Thermogravimetric analysis (TGA) curves of the CMC and CMC+Gly films with different concentrations of glycerol. (b) Differential scanning calorimetry (DSC) profiles of the CMC and CMC+Gly films.

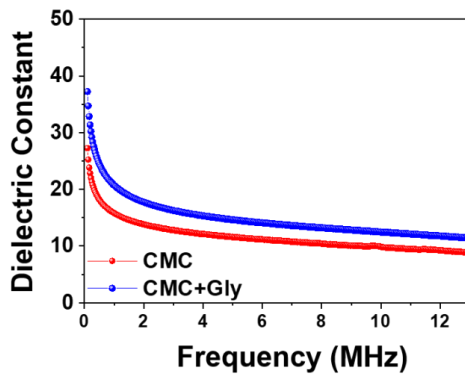


Figure 1.5. Variation in the dielectric constants of the CMC and CMC+Gly films as a function of the frequency.

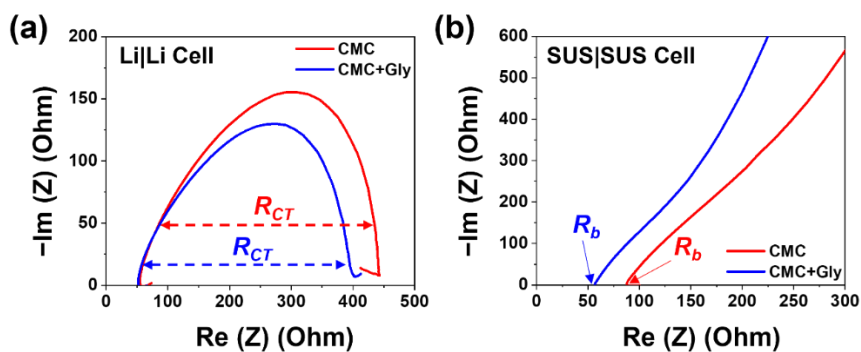


Figure 1.6. EIS plots for estimating the Li ion conductivity of polymeric membranes in the (a) Li symmetric and (b) SUS symmetric cells.

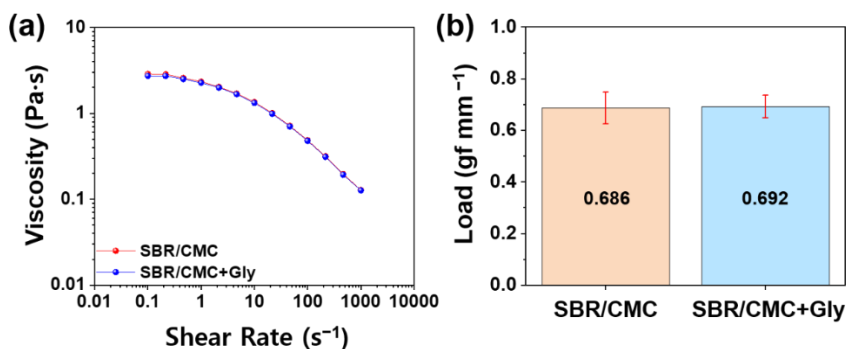


Figure 1.7. (a) Viscosity curves of the SBR/CMC and SBR/CMC+Gly slurries at various shear rates. (b) Results of the 180° peeling test of the SBR/CMC and SBR/CMC+Gly electrodes. Graphite loading = 8.1 mg cm⁻².

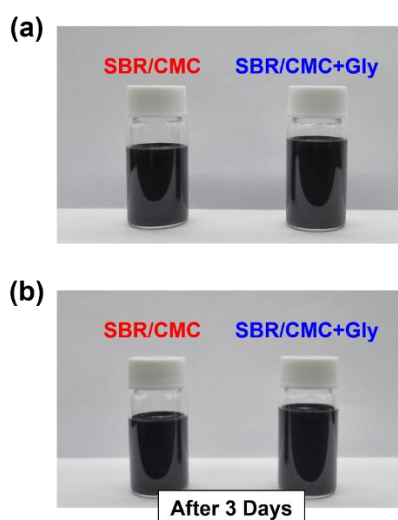


Figure 1.8. Phase stability test for the SBR/CMC and SBR/CMC+Gly slurries. (a) Photographs of the slurries (a) immediately after preparation and (b) after 3 days.

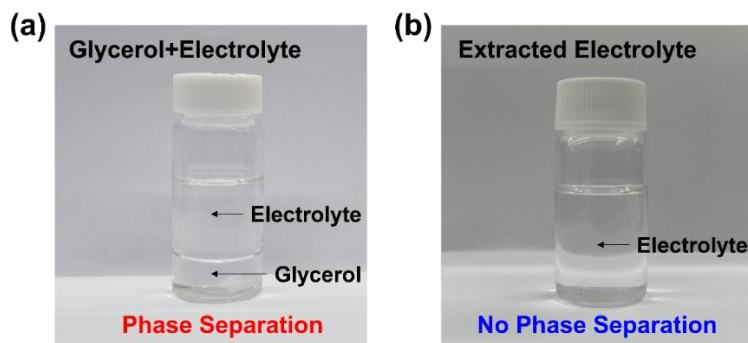


Figure 1.9. (a) Photograph of a mixture of glycerol and electrolyte after 3 days. (b) Photograph of the extracted electrolyte after immersing the CMC+Gly (1/1 weight ratio) film in the electrolyte for 3 days. An excess amount of glycerol was introduced to the CMC+Gly film to enable the phase separation to be clearly observed.

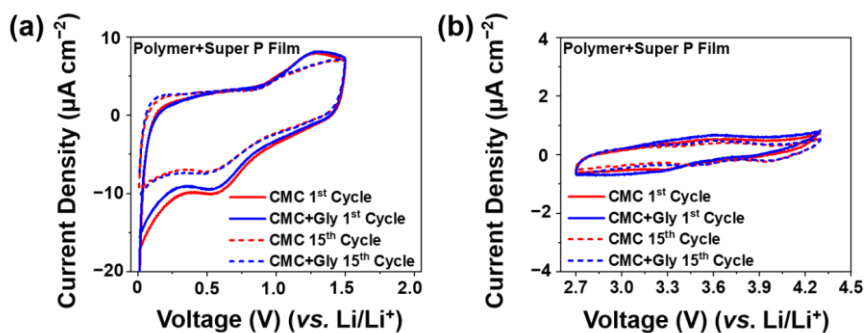


Figure 1.10. CV profiles of CMC and CMC+Gly at the 1st and 15th cycle with Super P (1:1 wt%) at 0.1 mV s⁻¹. The CV results in the potential range of (a) 0.01–1.5 V (vs. Li/Li⁺) and (b) 2.7–4.3 V (vs. Li/Li⁺).

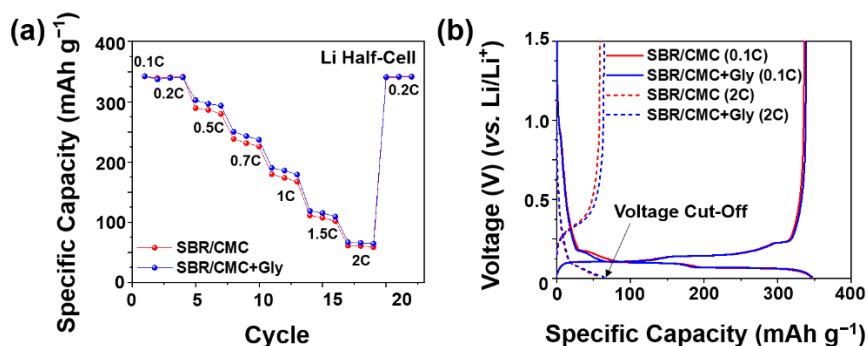


Figure 1.11. Electrochemical results of half-cells based on the SBR/CMC and SBR/CMC+Gly electrodes. (a) Rate capability at various C-rates and (b) corresponding galvanostatic charge-discharge profiles at 0.1C and 2C.

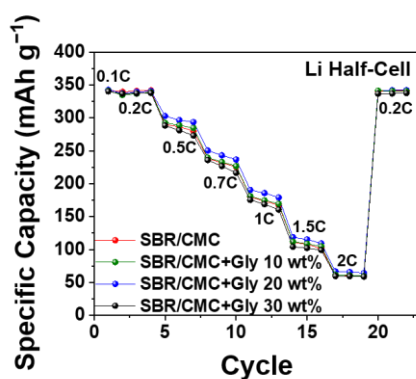


Figure 1.12. Half-cell rate capability of the SBR/CMC electrode and SBR/CMC+Gly electrodes with various glycerol contents to optimize the glycerol amount.

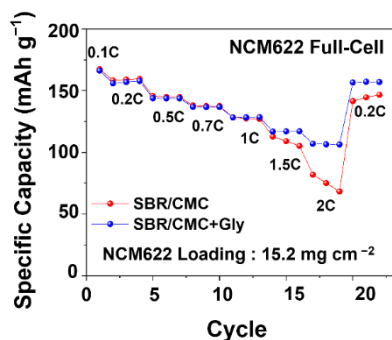


Figure 1.13. Rate capability results of the full-cells in which NCM622 cathodes are paired with graphite anodes containing SBR/CMC and SBR/CMC+Gly.

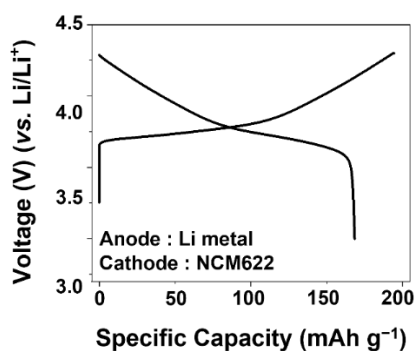


Figure 1.14. Initial profile of NCM622 in the half-cell configuration when scanned at 0.1C (1C = 170.4 mA g⁻¹).

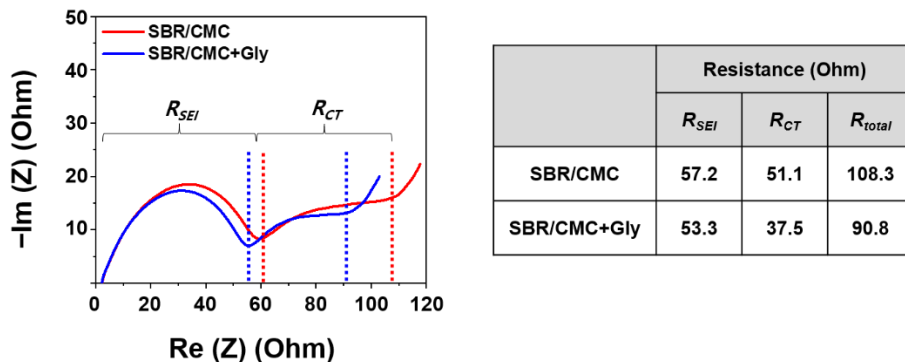


Figure 1.15. EIS profiles of the SBR/CMC and SBR/CMC+Gly electrodes after 5 cycles at 0.5C. Corresponding R_{SEI} and R_{CT} values (right).

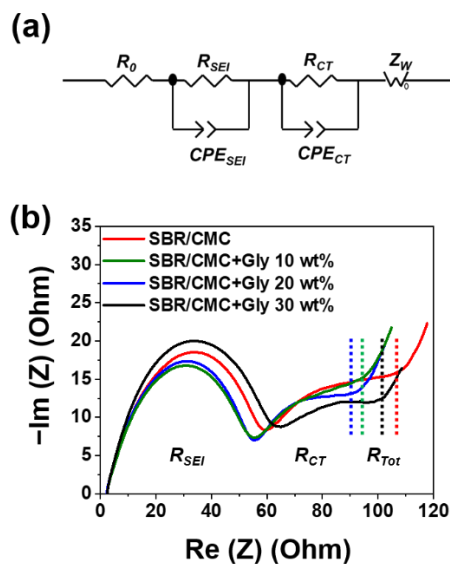


Figure 1.16. (a) Equivalent circuit for the EIS measurement. (b) EIS profiles of the SBR/CMC and SBR/CMC+Gly electrodes with different contents of glycerol.

Chapter 2. Elastic Zn^{2+} -Imidazole Coordination

Binder Network for Silicon Anodes

2.1 Introduction

In the battery community, considerable research has led to unambiguous consensus that a polymeric binder plays a critical role in the stable cycling of silicon (Si) anodes in lithium-ion batteries (LIBs).^[1] A variety of structural and compositional advancements in active materials, such as glass-type SiO_x ^[2] and alloy-type SiX_y ($\text{X}=\text{Fe}$, Mg , etc.)^[3] based on the adjustment of the elemental composition as well as on smart composite designs^[4] comprising Si and carbonaceous materials, have enabled the Si content in the electrode to be increased while achieving superior cyclability at the same time. Apart from the advancement in active material design, the incorporation of advanced polymeric binders further improved the key battery performance, thereby raising the status of Si anode technology in its entirety from the standpoint of commercialization.

The promising feature of Si anodes is the possibility they offer to increase the specific energy of a LIB cell by taking advantage of their high theoretical specific capacity ($>3000 \text{ mAh g}^{-1}$) and low operating potential ($\sim 0.3 \text{ V vs. Li/Li}^+$).^[5] The increased energy density translates into extending the time for which mobile information technology (IT) devices can be used and the distance electric vehicles (EVs) can be driven per charge. Nevertheless, several failure mechanisms arising from the immense volume change of Si during repeated charge-discharge cycles have long been identified^[6] as hurdles that need to be overcome. These failure mechanisms include pulverization of particles,

delamination of the electrode, and destabilization of the solid-electrolyte-interphase (SEI) layer.^[7] The difficulty with addressing these issues is that these mechanisms are often inter-related to one another in a way that once one mechanism is triggered, the other mechanisms are increasingly likely to occur.

Besides advanced binder designs,^[1a] a variety of strategies have been introduced to overcome the aforementioned problems of Si electrodes, targeting active material and electrolyte. From an active material design viewpoint, diverse nanostructures^[8] and composite designs^[9] were reported to buffer the volume change of Si. Additive engineering^[10] is most representative for electrolyte-based approaches, and in this direction, fluorine-containing compounds^[11] are remarkable to produce compact and stable SEI layer.

Clearly, binder design needs to take the structure and size of the active material into consideration. Although diverse nanostructured Si (nano-Si)^[12] with different morphologies has been studied widely, its low tap density, high cost, and large surface-to-volume ratio render it less attractive for use in practical cells. Instead, micrometer-sized silicon/carbon (Si/C) composites and SiO_x have been used most widely for commercial LIBs. Therefore, binder designs targeting these two classes of active material are of utmost priority.

The suitability of a polymeric binder is mainly assessed by its contribution to maintaining the structural integrity of the corresponding electrode. In this context, each polymer can be viewed by focusing on its functionality and chain structure.^[1a] From the viewpoint of functionality, active particle-to-binder interaction with high affinity is preferable to weak Van der Waals interaction to sustain the electrode during cycling. From the perspective of the chain structure, three-dimensional (3D) network structures are more favorable than their linear counterparts because of the superior ability of 3D networks to dissipate the stress created during the volume expansion of Si.^[1b] On a related note, the self-healing capability was recently recognized^[13] as a

useful concept to pursue because it can restore particle-to-binder interactions even when these interactions are disrupted when the volume of Si changes. For this purpose, noncovalent bonds with high binding affinity and highly elastic polymer structures were found^[14] to be effective. It is worthwhile noting that the binder system that is currently the most widely adopted in industry, and thus serves as a reference, is a styrene butadiene rubber/carboxymethyl cellulose (SBR/CMC) hybrid. Its popularity is attributable to the complementarity of its components to each other and their compatibility with the existing aqueous slurry-based manufacturing scheme. The advantages of this hybrid system are that CMC is highly adhesive to the carbonaceous surface and is suitable for controlling the viscosity of the slurry, while the SBR acts as a cushion to buffer the volume change of the active material. Nonetheless, when the Si content surpasses a certain portion (i.e., 10 wt%), unfortunately, the SBR/CMC binder is no longer able to sustain the integrity of the electrode. This shortcoming calls for the development of more advanced binder designs.

Along this line, various concepts including the implementation of polar functional groups,^[15] host-guest interactions,^[16] 3D cross-linked structures,^[17] and highly elastic polymer structures^[18] were recently demonstrated to extend the cycle life markedly. Especially, supramolecular chemistries turned out to be effective in maintaining the electrode integrity because their reversible noncovalent bonds can dynamically restore active particle-to-binder and binder-to-binder contacts, thus realizing self-healing. Among the various available noncovalent bonds, our investigation focuses on metal-ligand (M-L) coordination bonds. Our design was motivated by the fact that M-L bonds are one of the strongest noncovalent bonds, and their complexation is well defined based on the specific binding of a central metal ion with a limited pool of designated ligands.^[19] Thus, once incorporated into an appropriately designed structure, metal ions can be coordinated to carefully selected ligands that

protrude from polymer chains and can perform as the centers of dynamic crosslinks in a polymer network.^[20] We particularly intended to adhere to CMC, as its role as a viscosity enhancer is well established in the industry. Another reason for choosing CMC is to take advantage of its water solubility.^[21] With respect to the detailed design of the polymer, Zn(II)-imidazole coordination chemistry and its *in situ* crosslinking capability were exploited and applied to the CMC polymer such that the elasticity/plasticity of the final binder network could be tuned in a sophisticated manner.^[22] As a result of this binder design, when applied to a micrometer-sized Si/C composite electrode with a substantial areal capacity ($>3 \text{ mAh cm}^{-2}$), stable cycling performance was achieved in both half-cell and full-cell configurations.

2.2 Experimental section

Materials and chemicals. PEGDGE ($M_n = 500$), 1-(3-aminopropyl) imidazole, Na-CMC ($M_w = 250,000$) and PVDF ($M_w = 534,000$) were purchased from Sigma-Aldrich (USA). Ethanol was purchased from Samchun (South Korea). Zinc nitrate hexahydrate ($\text{Zn}(\text{NO}_3)_2 \cdot 6\text{H}_2\text{O}$) was purchased from Alfa Aesar (USA). The average particle size of the Si/C composite was $10 \mu\text{m}$. Super P was purchased from Timcal (Switzerland). A dialysis membrane tube with a molecular weight cut-off of 1 kDa was purchased from Membrane Filtration Products, Inc. (USA). N-methyl-2-pyrrolidone (NMP) was purchased from Junsei (Japan).

Synthesis of polymer. PEGDGE-Im was synthesized by introducing 9 g of PEGDGE and 3.6 g of 1-(3-aminopropyl) imidazole to 60 mL ethanol and stirred at 50°C for 4 h . The mixture was dialyzed against ethanol for 3 days using a dialysis membrane (MWCO, 1 kDa) to remove unreacted molecules.

After the dialysis, the mixture was lyophilized to yield the final product. **PEGDGE-Im-Zn²⁺** was synthesized by adding 2.14 g of zinc nitrate hexahydrate to the above-mentioned solution of **PEGDGE-Im** and stirred for 12 h. The molar ratio of imidazole and Zn²⁺ was 4:1. The same purification method as for **PEGDGE-Im** was used for the mixture and yielded a yellow transparent elastomeric material.

Characterization. Field-emission scanning electron microscopy (FE-SEM) (JSM-7800F Prime, JEOL, Japan) was used to characterize the morphology of the various electrodes. Energy dispersive spectrometry (EDS) mapping was performed to visualize the elemental distributions of the active material. ¹H NMR analysis (Bruker Avance III NMR 400 MHz) and FT-IR spectroscopy (TENSOR27, Bruker, Germany) were carried out to characterize the chemical structures. The molecular weight distribution and mean value of **PEGDGE-Im** were measured using matrix-assisted laser desorption ionization mass spectrometer (MALDI-TOF) (MALDI TOF Voyager DE-STR, Applied Biosystems, USA). The *T_g* was determined using DSC (PerkinElmer DSC 4000) at a ramping rate of 10 °C min⁻¹. Raman spectra were recorded on a Raman spectrometer II (DXR 2xi, Thermo, USA). For this analysis, polymer films were prepared on a glass slide and a 532 nm laser was used as the light source. ICP-AES (OPTIMA 8300, Perkin-Elmer, USA), ICP-MS (NexION 350D, Perkin-Elmer, USA), and SEM-EDS analyses were conducted to evaluate the content of Zn and its distribution in the polymer. The peeling tests were performed using a universal testing machine (UTM) (QM100s, QMESYS, South Korea). In the peeling tests, 3M double-sided tape was attached to the electrodes and peeled off at a rate of 25 mm min⁻¹ to evaluate the adhesion strength. The surface components of electrodes were analyzed using an X-ray photoelectron spectrometer (Axis Supra, Kratos, UK). Nanoindentation tests

were carried out using an ultra-precision surface mechanical analyzer (Anton Paar, Austria). For this analysis, samples were prepared by spin-coating polymers on a Si wafer at 3000 rpm for 100 s, followed by a drying step at 60 °C for 24 h. In the case of **CMC-PEG-Im-Zn²⁺**, the drying procedure differed and entailed drying at 130 °C in a vacuum oven for 4 h and subsequently at 60 °C under vacuum overnight. The indentation load was either 0.5 mN or 1 mN and the tests were repeated at five different positions on each electrode. Cross-sectional images of the electrodes were attained using a focused ion beam (FIB) (Helios G4, Thermo Fisher Scientific, USA). Electrodes were first dissected using a gallium (Ga) ion beam at 30 kV, and images of their cross-sections were captured *via* FE-SEM in the same FIB instrument.

Preparation of electrodes. Electrode preparation involved first preparing slurries containing Si/C, binder, and Super P in a weight ratio of 8:1:1. In this process, each binder was first dispersed in deionized water. For the SBR/CMC binder, the weight ratio between SBR and CMC was 1:1. For the SBR/CMC-PEG-Im-Zn²⁺ binder, the weight ratio among SBR, CMC, and PEGDGE-Im-Zn²⁺ was 5 : 4.5 : 0.5. The slurry for each electrode was cast on copper foil using the doctor blading method. In the case of the SBR/CMC-PEG-Im-Zn²⁺ and SBR/CMC-PEG-Im electrodes with active loadings of 3.67 and 3.65 mg cm⁻², respectively, the electrodes were dried in a vacuum oven at 130 °C for 4 h to allow thermal crosslinking to take place, followed by additional drying at 60 °C under vacuum overnight. The control electrodes based on PVDF and SBR/CMC underwent drying at 100 °C for 10 min and then at 60 °C under vacuum overnight. The active loadings of these control electrodes was 3.62 and 3.67 mg cm⁻², respectively. All electrodes were compressed to reach the density of 1.0–1.1 g cm⁻³. The assembly of full-cells

required the fabrication of cathodes consisting of NCA, PVDF, and Super P in a weight ratio of 90 : 5 : 5. For this electrode fabrication, the slurry based on NMP was cast onto aluminum foil, followed by drying at 60 °C under vacuum for one day. For full-cell assembly, the N/P ratio was set to 1.1 to provide a proper amount of excessive Li accommodation sites in the anode during the pre-cycle.

Electrochemical measurements. CR2032 coin cells were assembled in an Ar-filled glove box for all galvanostatic electrochemical tests. The electrode diameter was 10 mm in all cases. In the half-cells, Li metal foil with a 15 mm diameter was used as the reference/counter electrode. Polyethylene film (SK Innovation, South Korea) was used as a separator. The electrolyte comprised 1.0 M lithium hexafluorophosphate (LiPF_6) in ethylene carbonate (EC)/diethylene carbonate (DEC) in 1/1 volume ratio with 10 wt% fluoroethylene carbonate (FEC) (Welcos, South Korea). All electrochemical data were recorded on a battery cycler (WBCS 3000, WonATech, South Korea) at 25 °C. Before cycling, all cells were rested for 6 h. Prior to the half-cell tests, one pre-cycle was implemented at 0.1C to form a stable SEI layer, and subsequent cycles were at 0.5C. The potential range in both the pre-cycle and subsequent cycles was 0.01–1.5 V (vs. Li/Li^+), and each charge and discharge cycle was carried out in constant current (CC) mode. In the rate capability tests, each cell was subjected to various C-rates from 0.1C to 2.0C. The full-cell tests were conducted by using one pre-cycle at 0.1C and subsequent cycles were scanned at 0.5C in the potential range of 2.5–4.2 V in constant current constant voltage (CCCV) mode for charging and in CC mode for discharging. Electrochemical impedance spectroscopy (EIS) was employed using a potentiostat (VSP, Bio-Logic, France). The frequency ranged from 1 MHz to 0.1 Hz. Cyclic voltammetry (CV) tests were carried out at a scan rate of 0.05

mV s⁻¹ in the potential range of 0.01–1.5 V (vs. Li/Li⁺).

2.3 Result and discussion

Figure 2.1a illustrates the overall synthetic scheme to produce the M-L network. To this end, poly(ethylene glycol) diglycidyl ether (PEGDGE) was first reacted with 1-(3-aminopropyl) imidazole in a molar ratio of 2:1 *via* an epoxy-amine reaction to yield **PEGDGE-Im** dimers.^[23] The terminal epoxy groups in the dimers were subsequently reacted with 1-(3-aminopropyl) imidazole to form **PEGDGE-Im**. Zn²⁺ was then added to yield **PEGDGE-Im-Zn²⁺** in which Zn²⁺ and imidazole were coordinated in a 1:4 molar ratio. **CMC-PEG-Im-Zn²⁺** was finally obtained through a crosslinking reaction between **PEGDGE-Im-Zn²⁺** and CMC by exposure to heat. During electrode fabrication, this crosslinking can be achieved when the electrode is being dried (Figure 2.1b) and thus occurs *in situ*. The hydroxyl and carboxylate functional groups of CMC can be covalently linked^[24] with epoxy groups upon heating or under alkaline conditions, as presented in Figure 2.2. Consequently, **CMC-PEG-Im-Zn²⁺** engages in both covalent and noncovalent M-L complex crosslinking, which synergistically maintains the electrode integrity against the massive volume expansion of Si (Figure 2.1b).

The linkage of imidazole to PEGDGE was verified by ¹H nuclear magnetic resonance (NMR) analysis (Figure 2.3a). When dissolved in DMSO-*d*₆ solvent, chemical shifts at 6.86, 7.14, and 7.58 ppm, which are related to the hydrogen on the imidazole ring, were observed.^[25] The presence of the epoxy groups in **PEGDGE-Im**, which are required for its crosslinking to CMC, was also confirmed by Fourier-transform infrared (FT-IR) spectroscopy (Figure 2.4a) and ¹H NMR analysis (Figure 2.4b).^[26] The FT-IR spectra of PEGDGE-Im displayed peaks at 852 and 946 cm⁻¹ that are associated with the bending

vibration of the epoxy group, implying that the imidazole and epoxy groups were successfully integrated with the designated polymer architectures. The mean molecular weight of **PEGDGE-Im** was 1310.81 Da (Figure 2.5), which infers that the number of units (n value) in this polymer is between 2 and 3.

Figure 2.3b visually captures the Zn^{2+} -imidazole complexation upon the addition of Zn^{2+} to **PEGDGE-Im**. Before the complexation, **PEGDGE-Im** had the fluency of a viscous liquid when the vial was held upside down (Figure 2.3b, left), whereas a yellowish gel formed once Zn^{2+} was added (Figure 2.3b, right). Moreover, M-L complexation affects the mobility of the polymer chains such that the glass transition temperature (T_g) of the polymer is raised. According to the differential scanning calorimetry (DSC) results (Figure 2.3c), **PEGDGE-Im** and **PEGDGE-Im-Zn²⁺** exhibited T_g at -35.9 and -30.2 °C, respectively. The elevated T_g of **PEGDGE-Im-Zn²⁺** is attributed to weakened chain mobility owing to crosslinking *via* M-L complex formation.^[27] The chemical bonds were further investigated using Raman spectroscopy (Figure 2.3d). M-L complexation in **PEGDGE-Im** manifested itself in the form of peak shifts from 1284, 1398, and 1506 cm^{-1} to 1294, 1408, and 1531 cm^{-1} , respectively (Figure 2.3d). The blue shifts can be explained^[28] by the strengthened chemical bonds of the imidazole ring, including the C=C bond, as Zn^{2+} coordinates to the imidazole. In fact, it is well accepted that M-L causes the wavenumbers corresponding to the imidazole ring to undergo blue shift by 5–20 cm^{-1} compared with those of its metal-free configuration.^[28b, 29] The peaks of the imidazole- Zn^{2+} complex, when not bonded to PEGDGE, were consistently observed to undergo blue shift (Figure 2.6). In addition, scanning electron microscopy-energy dispersive spectrometry (SEM-EDS) (Figure 2.7) indicates that Zn is uniformly distributed in **PEGDGE-Im-Zn²⁺**, and its content was found to be 42.15 g L⁻¹ by inductively coupled plasma-atomic emission spectrometry (ICP-AES).

As described above, **PEGDGE-Im-Zn²⁺** is designed to crosslink with CMC *in situ* upon the application of thermal treatment to dry the electrode. The existence of thermal crosslinking was reflected in the solubility of this compound in water. Interestingly, a blend of **PEGDGE-Im-Zn²⁺** and CMC was fully water-soluble (Figure 2.3e, left), whereas their thermally crosslinked form remained water-insoluble even after stirring for 3 days (Figure 2.3e, right). This insolubility can be understood on the basis of the epoxy-to-carboxylate and epoxy-to-hydroxyl covalent interactions that impede the dispersion of the individual polymer chain in **CMC-PEG-Im-Zn²⁺**, transforming the entire solution into a gel-like substance.^[30] To check the stability of M-L complexation after the crosslinking to CMC, Raman analysis was conducted (Figure 2.8). According to the Raman spectroscopy results, a similar level of blue shift characteristic of Zn²⁺-Im complexation was observed for both before and after the crosslinking to CMC (Figures 3.3d, 3.8), suggesting high stability of M-L complex throughout the synthesis.

Assessment of the adhesion of electrodes *via* a 180° peeling test over a displacement of 5–15 mm indicated that the adhesion force of the SBR/**CMC-PEG-Im-Zn²⁺** electrode was higher than that of the SBR/CMC- and poly(vinylidene fluoride) (PVDF)-based ones. Specifically, the adhesion force of the SBR/**CMC-PEG-Im-Zn²⁺**, SBR/CMC, and PVDF electrodes was 4.83, 3.79, and 2.07 gf mm⁻¹, respectively (Figure 2.3f). The superior adhesion of the SBR/**CMC-PEG-Im-Zn²⁺** results from the M-L crosslinks that tighten the active particle network, in addition to the well-known interaction of CMC with the carbon surface of Si/C.^[1a] Additionally, inductively coupled plasma-mass spectrometry (ICP-MS) showed that the SBR/**CMC-PEG-Im-Zn²⁺** electrode contained a concentration of 300.97 mg kg⁻¹ of Zn²⁺.

Considering that the mechanical properties of the binder play a crucial role in maintaining the integrity of the electrode, nanoindentation analysis was

carried out for bare polymer films. When subjected to a nanoindentation test, a polymer film generally deforms in one of the three possible ways: plastic, elastic, or viscoelastic.^[31] In the case of plastic deformation, the absence of recovery during unloading is represented by a vertical profile on the load vs. indentation depth graph. By contrast, elastic deformation involves the opposite behavior such that the loading and unloading profiles overlap, reflecting the perfect reverse trajectory of unloading compared to that of loading. Viscoelastic behavior lies between plastic and elastic deformation, leading to a curved unloading profile that is offset from the loading profile.

The loading-unloading profiles of **CMC-PEG-Im-Zn²⁺** and CMC with respect to indentation depth are presented in Figure 2.9a, b, respectively. The maximum penetration depth is referred to as the indentation depth when the maximum load (0.5 mN in our case) is reached, whereas the recovered length is defined as the restored distance upon complete unloading. As a descriptor to quantitatively assess the elasticity of a polymer film, we define the “elastic recovery ratio” as:

$$\text{Elastic recovery ratio} = \frac{\text{Recovered length}}{\text{Max penetration depth}} \quad (1)$$

The **CMC-PEG-Im-Zn²⁺** film (Figure 2.9a) exhibited an elastic recovery ratio of 0.46, which is higher than that of the CMC film (0.41) (Figure 2.9b).^[32]

The elasticity can also be assessed in terms of the degree of energy conservation. As the integrated area below the load vs. indentation depth curve corresponds to the energy exerted during the indenting period or the energy restored during the unindenting period, the difference in the integrated areas of the loading and unloading curves (hatched areas in Figure 2.9c, d) indicate plastic work (P). On the contrary, the integrated areas below the unloading

curve represent elastic work (E) (shaded areas in Figure 2.9c, d). The P and E can also be interpreted as the lost energy absorbed by the material under testing and the energy recovered (thus reversible) by the elasticity of the material, respectively.^[33] According to this energy analysis, the P and E values of the CMC film were 23.6 and 9.8 pJ, respectively, whereas those of the **CMC-PEG-Im-Zn²⁺** film were 25.6 and 13.9 pJ, respectively. Because the elasticity of a film is related to the relative contributions of these two parameters, the E/P ratio is of interest to us:

$$\text{E/P ratio} = \frac{\text{elastic work}}{\text{plastic work}} \quad (2)$$

The E/P ratios of the CMC and **CMC-PEG-Im-Zn²⁺** films were 0.41 and 0.54, respectively, for a maximum load of 0.5 mN. The well-known stiff properties of CMC would serve as the origin of the observed lower E/P ratio. By contrast, the Zn²⁺-imidazole complex as well as the PEG chains endow the polymer network with flexibility, which is responsible for the higher E/P ratio of **CMC-PEG-Im-Zn²⁺**. In particular, the reversible character of the Zn²⁺-imidazole coordination bonds allows for their recovery even when the bonds are perturbed during indentation, which is observed in the form of the large amount of elastic work associated with the corresponding polymer film.

The electrochemical stability of the **CMC-PEG-Im-Zn²⁺** binder was assessed by conducting a cyclic voltammetry (CV) test (Figure 2.10a). The conductive agent, Super P, was also included in the binder films in a weight ratio of 1:1 to complement the electronic conductivity. The CV profiles of the **CMC-PEG-Im-Zn²⁺** film at the 1st, 10th, and 35th cycle indicate that cathodic peaks at 0.7 and 1.6 V, associated with the decomposition of the electrolyte, are present during the first cycle.^[34] However, signals related to the reduction of

Zn^{2+} were absent, which implies that the Zn^{2+} in the **CMC-PEG-Im- Zn^{2+}** remained in the original valence state without undergoing a substantial redox reaction. X-ray photoelectron spectroscopy (XPS) analysis further supports the stable nature of Zn^{2+} during cycling (Figure 2.11). The **CMC-PEG-Im- Zn^{2+}** electrode displayed a peak at 1022.2 eV in its Zn 2p_{3/2} spectra, indicating^[35] that Zn^{2+} in **CMC-PEG-Im- Zn^{2+}** maintained its bivalency during cycling and supporting the robust character of the M-L complex in our binder. This phenomenon can also be interpreted to suggest that electron transfer in the Zn^{2+} -imidazole complex is limited to the electrode environment. Similarly, the robustness of the complex was verified by FT-IR analysis that showed largely consistent results for the films before and after CV cycles (Figure 2.12). Overall, the **CMC-PEG-Im- Zn^{2+}** binder proved to be electrochemically inert in the given potential range of the anode (Figure 2.13).

To determine the effect of the binder on the key electrochemical performance, Si/C electrodes with different binders were galvanostatically evaluated under the coin half-cell setting in the potential range of 0.01–1.5 V (vs. Li/Li⁺). Each of the electrodes consisted of Si/C active material, binder, and Super P in a weight ratio of 8:1:1. The areal capacity was set to 2.2–2.4 mAh cm⁻² at 0.1C (1C=650 mA g⁻¹) (Figure 2.10b).^[36] With this areal capacity, the SBR/**CMC-PEG-Im- Zn^{2+}** electrode exhibited sustainable cyclability without any capacity loss at all for 200 cycles when operated at 0.5C. By contrast, the SBR/CMC electrode lost its capacity abruptly at around the 125th cycle presumably owing to electrolyte depletion.^[18, 37] In the case of the PVDF electrode, the capacity decayed steadily from the beginning, which can be explained by the weak Van der Waals force that characterizes the interaction of PVDF with Si/C. The capacity retentions of the SBR/**CMC-PEG-Im- Zn^{2+}** , SBR/CMC, and PVDF electrodes after 200 cycles were 100.8%, 40.4%, and 69.9%, respectively. The retention of the SBR/**CMC-PEG-Im- Zn^{2+}** electrode

in excess of 100% is attributed to an interfacial activation process that would require further investigation to fully understand. A similar trend was observed for the Coulombic efficiency (CE) during cycling. The CE of the **SBR/CMC-PEG-Im-Zn²⁺** electrode rose more drastically such that the CE at the 2nd, 10th, 20th, and 50th cycles was 96.93%, 99.77%, 99.84%, and 99.87%, respectively (Figure 2.10c). On the contrary, the CEs of the SBR/CMC and PVDF electrodes saturated at 99.46% and 99.09%, respectively, after the 50th and 60th cycles. The average CEs of the **SBR/CMC-PEG-Im-Zn²⁺**, SBR/CMC, and PVDF electrodes for cycles 61–200 were 99.91%, 99.42%, and 99.20%, respectively. The superior CE of the **SBR/CMC-PEG-Im-Zn²⁺** electrode stems from the intimate active particle-to-binder interactions that are maintained even during the immense volume change of Si/C by taking advantage of the elasticity of the binder. These intimate contacts stabilize the SEI layer during cycling with controlled electrolyte decomposition such that electrons from the electrode are merely wasted. To elucidate the role of Zn²⁺ in the M-L complexes, the **SBR/CMC-PEG-Im** electrode was tested without Zn²⁺-coordination (Figure 2.14). The capacity of this Zn²⁺-free electrode decayed sharply at around the 130th cycle, thereby reflecting electrolyte depletion owing to uncontrolled interfacial side reactions and reconfirming the importance of Zn²⁺-imidazole complexation. This sharp decay was reflected in a drop in its CE profile; the CE value of the **SBR/CMC-PEG-Im** electrode began to drop at the nearly same cycling point around the 130th cycle (Figure 2.15).

The rate capability of all the electrodes was assessed by varying the C-rate from 0.1C to 2C (Figure 2.10d). All the electrodes began operating with similar initial capacities around 640 mAh g⁻¹ at 0.1C, but the **SBR/CMC-PEG-Im-Zn²⁺** electrode was noticeably more effective at preserving the capacity at high C-rates. For example, at 2C, the average capacities of the **SBR/CMC-PEG-Im-Zn²⁺**, SBR/CMC, and PVDF electrodes were 261.8, 248.6, and 231.8

mAh g⁻¹, respectively. In addition, the capacity of the SBR/CMC-PEG-Im-Zn²⁺ electrode was fully recovered when the current rate returned to 0.1C. This superior rate performance is attributed to the elastic nature of the SBR/CMC-PEG-Im-Zn²⁺ network, which tightens the interparticle contacts to enhance the ionic and electronic transport at the interface.^[14c, 18c, 38] In the same vein, the elasticity of SBR/CMC-PEG-Im-Zn²⁺ renders the interface of the electrode less prone to degradation during cycling at various C-rates. Beside the elastic behavior, the PEG units in CMC-PEG-Im-Zn²⁺ contribute to Li-ion transport and thus the enhanced rate performance by offering hopping sites for Li ions. This observation was consistent with the electrochemical impedance spectroscopy (EIS) results when measured after 10 cycles (Figure 2.16). The SBR/CMC-PEG-Im-Zn²⁺ electrode produced smaller semi-circles corresponding to SEI layer resistance (R_{SEI}) and charge transfer resistance (R_{CT}), both of which are critical for good rate performance.

The cycling test was extended to cover a greater number of cycles, namely 400 (Figure 2.10e). During this test, the Li metal counter electrode was replaced with a fresh one after 200 cycles to enable us to exclude the effect of the degradation of the Li counter electrode related to Li dendrite growth.^[18a] The SBR/CMC-PEG-Im-Zn²⁺ electrode with an areal capacity of 2.16 mAh cm⁻² retained 96.2% of its initial capacity when cycled at 0.5C. The average CE in the periods before and after the Li metal replacement was 99.87% and 99.91%, respectively.

The practical viability of SBR/CMC-PEG-Im-Zn²⁺ was examined by carrying out coin full-cell tests by pairing the electrode with a LiNi_{0.8}Co_{0.15}Al_{0.05}O₂ (NCA) cathode with a specific capacity of 183.1 mAh g⁻¹ at 0.1C (Figure 2.17). The cathode was composed of NCA, PVDF, and Super P in a weight ratio of 90:5:5, and the active material loading was either 17.18 mg cm⁻² or 26.83 mg cm⁻². The full-cells based on these two different loadings

delivered 2.6 and 4.3 mAh cm⁻² at 0.1C, respectively (Figure 2.18a). The capacity ratio between the anode and cathode, namely the n/p ratio, was set to 1.1. The SBR/CMC-PEG-Im-Zn²⁺ full-cell with the lower NCA loading exhibited good cycling behavior such that 81.5% of the original capacity of 2.5 mAh cm⁻² was retained after 150 cycles at 0.5C (Figure 2.18b). This performance was superior to that of the SBR/CMC and SBR/CMC-PEG-Im full-cells that preserved 74.6% and 78.2%, respectively, after the same number of cycles (Figure 2.19). Remarkably, the CE of the SBR/CMC-PEG-Im-Zn²⁺ full-cell rose sharply from the beginning and surpassed 99.9% at the 40th cycle. A SBR/CMC-PEG-Im-Zn²⁺ full-cell with the higher NCA loading also preserved 74.7% of the initial capacity after 150 cycles (Figure 2.18c). It should be noted that the cycle life of full-cells could be further improved by employing technical know-how of the various conditions related to cell manufacturing, such as the n/p ratio and viscosity of the slurry. Our study simply aims to demonstrate the practical viability of CMC-PEG-Im-Zn²⁺.

Cross-sectional SEM was employed to monitor the thickness and morphology of the SBR/CMC-PEG-Im-Zn²⁺ electrode during electrochemical cycling (Figure 2.20). In the pristine state, both the SBR/CMC and SBR/CMC-PEG-Im-Zn²⁺ electrodes had similar thicknesses of approximately 38 μm (Figure 2.21). However, the thicknesses of these electrodes became clearly distinct after the 30th delithiation in that they increased to 51 μm (Figure 2.20a) and 43 μm (Figure 2.20c), respectively. This change in the relative thickness originated from the different levels of SEI stability,^[18a, 18c, 39] as revealed by magnified images of the SEI (Figure 2.20b, d). In the case of the SBR/CMC electrode, the interparticle space was completely filled with the SEI layer (Figure 2.20b), which provides direct evidence of an unstable interface. By stark contrast, a significant portion of the interparticle space of the SBR/CMC-PEG-Im-Zn²⁺ electrode remained void (Figure 2.20d) as the binder contributed

greatly to retaining the interparticle contacts. The same trend was observed after 135 cycles (Figure 2.22). The bulk-scale swelling of the electrodes, measured by a micrometer, also reflects the effect of the binder; the thicknesses of the SBR/CMC and SBR/CMC-PEG-Im-Zn²⁺ electrodes increased by 18% and 11% after 30 cycles, respectively, compared to their pristine states (Figure 2.20e). It is reminded that electrode swelling is a critical parameter in full-cell design and thus affects the specific energy of a cell.

Our combined results serve to corroborate that the superior electrochemical performance of the SBR/CMC-PEG-Im-Zn²⁺ binder is ascribed to its high elasticity. We portray that this binder network is more effectively able to tolerate the volume change of the active material by utilizing the reversible bonding character of the Zn²⁺-imidazole complex and the flexibility of PEG (Figure 2.23a). CMC does not have this capability of buffering the volume change of Si because the polymer chains are not chemically interconnected. As a result, upon experiencing repeated charge-discharge cycles, the CMC polymer network ruptures as it is incapable of absorbing the stress originating from the volume change. Hence, “dynamic crosslinking” is the key to the superior performance of the SBR/CMC-PEG-Im-Zn²⁺ binder. The mechanical robustness of CMC-PEG-Im-Zn²⁺ was revealed when a film of this compound was subjected to repeated bending-unbending motion. Even after the CMC-PEG-Im-Zn²⁺ film was repeatedly bent 10 times, the original integrity of the film was maintained (Figure 2.23b). This behavior contrasts that of its CMC counterpart, which ruptured immediately after far weaker elongation stress was applied (Figure 2.23c).

2.4 Conclusion

In summary, we demonstrated the Zn²⁺-imidazole complex as a useful

crosslinking component to realize a binder with outstanding elasticity for Si/C composite electrodes. Crosslinking is accomplished in situ during the drying step of electrode preparation such that the dispersion of the binder throughout the electrode does not present a problem. The high elasticity of **CMC-PEG-Im-Zn²⁺** maintains tight interparticle contacts during cycling and enables the interface to remain stable and to offer high and consistent ionic conductivity. The recoverable nature of Zn²⁺-imidazole coordination bonds is also beneficial for sustaining the electrode integrity during the huge volume change Si/C undergoes, and this benefit is closely linked to its extended cycle life. This study highlights the significance of reversible noncovalent crosslinks as generally useful tools for designing a binder that targets high capacity battery electrodes that are adversely affected by a large volume change.

2.5 References

- [1] a) T.-w. Kwon, J. W. Choi and A. Coskun, *Chem. Soc. Rev.* **2018**, 47, 2145; b) T.-w. Kwon, J. W. Choi and A. Coskun, *Joule* **2019**, 3, 662; c) J. Lopez, D. G. Mackanic, Y. Cui and Z. Bao, *Nat. Rev. Mater.* **2019**, 4, 312.
- [2] a) T. Chen, J. Wu, Q. Zhang and X. Su, *J. Power Sources* **2017**, 363, 126; b) Z. Liu, Q. Yu, Y. Zhao, R. He, M. Xu, S. Feng, S. Li, L. Zhou and L. Mai, *Chem. Soc. Rev.* **2019**, 48, 285; c) S. J. Lee, H. J. Kim, T. H. Hwang, S. Choi, S. H. Park, E. Deniz, D. S. Jung and J. W. Choi, *Nano Lett.* **2017**, 17, 1870; d) S. Choi, D. S. Jung and J. W. Choi, *Nano Lett.* **2014**, 14, 7120.
- [3] a) N. Fukata, M. Mitome, Y. Bando, W. Wu and Z. L. Wang, *Nano Energy* **2016**, 26, 37; b) J. Chen, H. Zhao, J. He and J. Wang, *Rare Metals* **2011**,

30, 166.

[4] a) X. Shen, Z. Tian, R. Fan, L. Shao, D. Zhang, G. Cao, L. Kou and Y. Bai, *J. Energy Chem.* **2018**, 27, 1067; b) S. Chae, S.-H. Choi, N. Kim, J. Sung and J. Cho, *Angew. Chem. Int. Ed.* **2020**, 59, 110.

[5] a) S. Chae, M. Ko, K. Kim, K. Ahn and J. Cho, *Joule* **2017**, 1, 47; b) B. Dunn, H. Kamath and J.-M. Tarascon, *Science* **2011**, 334, 928.

[6] a) R. A. Huggins, *J. Power Sources* **1999**, 13, 81-82; b) M. T. McDowell, S. W. Lee, W. D. Nix and Y. Cui, *Adv. Mater.* **2013**, 25, 4966.

[7] J. W. Choi and D. Aurbach, *Nat. Rev. Mater.* **2016**, 1, 1.

[8] a) B. Zhu, X. Wang, P. Yao, J. Li and J. Zhu, *Chem. Sci.* **2019**, 10, 7132; b) A. Magasinski, P. Dixon, B. Hertzberg, A. Kvit, J. Ayala and G. Yushin, *Nat. Mater.* **2010**, 9, 353; c) W. C. Cho, H. J. Kim, H. I. Lee, M. W. Seo, H. W. Ra, S. J. Yoon, T. Y. Mun, Y. K. Kim, J. H. Kim, B. H. Kim, J. W. Kook, C.-Y. Yoo, J. G. Lee and J. W. Choi, *Nano Lett.* **2016**, 16, 7261.

[9] a) N. Kim, S. Chae, J. Ma, M. Ko and J. Cho, *Nat. Commun.* **2017**, 8, 812; b) H. M. Jeong, S. Y. Lee, W. H. Shin, J. H. Kwon, A. Shakoor, T. H. Hwang, S. Y. Kim, B. -S. Kong, Y. M. Lee, J. K. Kang and J. W. Choi, *RSC Adv.* **2012**, 2, 4311; c) I. H. Son, J. H. Park, S. Kwon, S. Park, M. H. Rummeli, A. Bachmatiuk, H. J. Song, J. Ku, J. W. Choi, J.-m. Choi, S. -G. Doo and H. Chang, *Nat. commun.* **2015**, 6, 7393; d) F. Luo, B. Liu, J. Zheng, G. Chu, K. Zhong, H. Li, X. Huang and L. Chen, *J. Electrochem. Soc.* **2015**, 162, A2509; e) D. S. Jung, T. H. Hwang, J. H. Lee, H. Y. Koo, R. A. Shakoor, R. Kharaman, Y. N.

Jo, M. -S. Park and J. W. Choi, *Nano Lett.* **2014**, *14*, 4418.

[10] a) A. M. Haregewoin, A. S. Wotango, B.-J. Hwang, *Energy Environ. Sci.* **2016**, *9*, 1955; b) C. Xu, F. Lindgren, B. Philippe, M. Gorgoi, F. Bjorefors, K. Edstrom and T. Gustafsson, *Chem. Mater.* **2015**, *27*, 2591; c) Y. Horowitz, H.-L. Han, F. A. Soto, W. T. Ralston, P. B. Balbuena and G. A. Somorjai, *Nano Lett.* **2018**, *18*, 1145; d) A. Schiele, B. Breitung, T. Hatsukade, B. B. Berkes, P. Hartmann, J. Janek and T. Brezesinski, *ACS Energy Lett.* **2017**, *2*, 2228.

[11] a) J. Chen, X. Fan, Q. Li, H. Yang, R. Khoshi, Y. Xu, S. Hwang, L. Chen, X. Ji, C. Yang, H. He, C. Wang, E. Garfunkel, D. Su, O. Borodin and C. Wang, *Nat. Energy* **2020**, *3*, 386; b) G. -B. Han, J. -N. Lee, J. W. Choi and J. - K. Park, *Electrochim. Acta* **2011**, *56*, 8997.

[12] a) H. Wu and Y. Cui, *Nano Today* **2012**, *7*, 414; b) C. K. Chan, H. Peng, G. Liu, K. McIlwrath, X. F. Zhang, R. A. Huggins and Y. Cui, *Nat. Nanotechnol.* **2008**, *3*, 31.

[13] a) Z. Xu, J. Yang, T. Zhang, Y. Nuli, J. Wang and S.-i. Hirano, *Joule* **2018**, *2*, 950; b) C. Luo, X. Fan, Z. Ma, T. Gao and C. Wang, *Chem* **2017**, *3*, 1050; c) C. Wang, H. Wu, Z. Chen, M. T. McDowell, Y. Cui and Z. Bao, *Nat. Chem.* **2013**, *5*, 1042.

[14] a) A. Magasinski, B. Zdyrko, I. Kovalenko, B. Hertzberg, R. Burtovyy, C. F. Huebner, T. F. Fuller, I. Luzinov and G. Yushin, *ACS Appl. Mater. Interfaces* **2010**, *2*, 3004; b) Q. Huang, J. Song, Y. Gao, D. Wang, S. Liu, S. Peng, C. Usher, A. Goliaszewski and D. Wang, *Nat. Commun.* **2019**, *10*, 5586;

- c) B. Chang, J. Kim, Y. Cho, I. Hwang, M. S. Jung, K. Char, K. T. Lee, K. J. Kim and J. W. Choi, *Adv. Energy Mater.* **2020**, *10*, 2001069.
- [15] a) I. Kovalenko, B. Zdyrko, A. Magasinski, B. Hertzberg, Z. Milicev, R. Burtovyy, I. Luzinov and G. Yushin, *Science* **2011**, *334*, 75; b) J. Guo and C. Wang, *Chem. Commun.* **2010**, *46*, 1428; c) J. Li, R. B. Lewis and J. R. Dahn, *Electrochem. Solid St.* **2007**, *10*, A17.
- [16] T.-w. Kwon, Y. K. Jeong, E. Deniz, S. Y. AlQaradawi, J. W. Choi and A. Coskun, *ACS Nano* **2015**, *9*, 11317.
- [17] a) J. Song, M. Zhou, R. Yi, T. Xu, M. L. Gordin, D. Tang, Z. Yu, M. Regula and D. Wang, *Adv. Funct. Mater.* **2014**, *24*, 5904; b) B. Liu, P. Soares, C. Checkles, Y. Zhao and G. Yu, *Nano Lett.* **2013**, *13*, 3414.
- [18] a) S. Choi, T.-w. Kwon, A. Coskun and J. W. Choi, *Science* **2017**, *357*, 279; b) C. Milroy and A. Manthiram, *Adv. Mater.* **2016**, *28*, 9744; c) Y. Cho, J. Kim, A. Elabd, S. Choi, K. Park, T.-w. Kwon, J. Lee, K. Char, A. Coskun and J. W. Choi, *Adv. Mater.* **2019**, *31*, 1905048.
- [19] a) M. J. Harrington, A. Masic, N. H.-Andersen, J. H. Waite and P. Fratzl, *Science* **2010**, *328*, 216; b) Y. Shi, M. Wang, C. Ma, Y. Wang, X. Li and G. Yu, *Nano Lett.* **2015**, *15*, 6276; c) T. Devic, B. Lestriez and L. Roue, *ACS Energy Lett.* **2019**, *4*, 550.
- [20] a) Z. Tang, J. Huang, B. Guo, L. Zhang and F. Liu, *Macromolecules* **2016**, *49*, 1781; b) D. Mozhdghi, J. A. Neal, S. C. Grindy, Y. Cordeau, S. Ayala, N. H.-Andersen and Z. Guan, *Macromolecules* **2016**, *49*, 6310.

- [21] J.-T. Li, Z.-Y. Wu, Y.-Q. Lu, Y. Zhou, Q.-S. Huang, L. Huang and S.-G. Sun, *Adv. Energy. Mater.* **2017**, 7, 1701185.
- [22] a) E. Filippidi, T. R. Cristiani, C. D. Eisenbach, J. H. Waite, J. N. Israelachvili, B. K. Ahn and M. T. Valentine, *Science* **2017**, 358, 502; b) L. Montero de Espinosa, W. Meesorn, D. Moatsou and C. Weder, *Chem. Rev.* **2017**, 117, 12851.
- [23] J. Liu, Y. Liu, Y. Wang, J. Zhu, J. Yu and Z. Hu, *Mater. Today Commun.* **2017**, 13, 282.
- [24] a) D. Lee, H. Park, A. Goliaszewski, Y.-k. Byeun, T. Song and U. Paik, *Ind. Eng. Chem. Res.* **2019**, 58, 8123; b) T. Vidil, F. Tournilhac, S. Musso, A. Robisson and L. Leibler, *Prog. Polym. Sci.* **2016**, 62, 126.
- [25] X. Cui, Y. Song, J.-P. Wang, J.-K. Wang, Q. Zhou, T. Qi and G. L. Li, *Polymer* **2019**, 174, 143.
- [26] a) H. Kono, T. Nakamura, H. Hashimoto and Y. Shimizu, *Carbohydr. Polym.* **2015**, 128, 11; b) N. Wang, Y. Guo, L. Wang, X. Liang, S. Liu and S. Jiang, *Analyst* **2014**, 139, 2531; c) D. Duraibabu, M. Alagar and S. A. Kumar, *RSC Adv.* **2014**, 4, 40132.
- [27] J. Zhang, Z. Huang and D. Liu, *Appl. Surf. Sci.* **2017**, 426, 796.
- [28] a) A. Torreggiani and A. Tinti, *Metallomics* **2010**, 2, 246; b) H. Takeuchi, *Biopolymers* **2003**, 72, 305.
- [29] D. S. Caswell and T. G. Spiro, *J. Am. Chem. Soc.* **1986**, 108, 6470.

- [30] J. Maitra and V. K. Shukla, *American J. Polymer Sci.* **2014**, *4*, 25.
- [31] B. J. Briscoe, L. Fiori and E. Pelillo, *J. Phys. D: Appl. Phys.* **1998**, *31*, 2395.
- [32] a) H. Jabir, A. Fillon, P. Castany and T. Gloriant, *Phys. Rev. Materials* **2019**, *3*, 063608; b) I. S. Vinoth, S. Detwal, V. Umasankar and A. Sarma, *Tribol. Mater. Surf. & Interf.* **2019**, *13*, 31.
- [33] a) N. Kikuchi, M. Kitagawa, A. Sato, E. Kusano, H. Nanto and A. Kinbara, *Surf. Coat. Tech.* **2000**, *126*, 131; b) S. A.-Roncancio, E. R.-Parra, D. M. D.-Narvaez, D. F. A.-Mateus and M. M. G.-Hermida, *DYNA* **2014**, *81*, 102.
- [34] A. Wang, S. Kadam, H. Li, S. Shi and Y. Qi, *npj Comput. Mater.* **2018**, *4*, 15.
- [35] E. Diler, B. Lescop, S. Rioual, G. N. Vien, D. Thierry and B. Rouvellou, *Corros. Sci.* **2014**, *79*, 83.
- [36] W. Wei, W. Ye, J. Wang, C. Huang, J.-B. Xiong, H. Qiao, S. Cui, W. Chen, L. Mi and P. Yan, *ACS. Appl. Mater. Interfaces* **2019**, *11*, 32269.
- [37] S. Komaba, N. Yabuuchi, T. Ozeki, Z.-J. Han, K. Shimomura, H. Yui, Y. Katayama and T. Miura, *J. Phys. Chem. C* **2012**, *116*, 1380.
- [38] H. Zhang, Z. Lv, Q. Liang, H. Xia, Z. Zhu, W. Zhang, X. Ge, P. Yuan, Q. Yan and X. Chen, *Batteries & Supercaps* **2020**, *3*, e1900136.
- [39] S. Jiang, B. Hu, Z. Shi, W. Chen, Z. Zhang and L. Zhang, *Adv. Funct. Mater.* **2020**, *30*, 1908558.

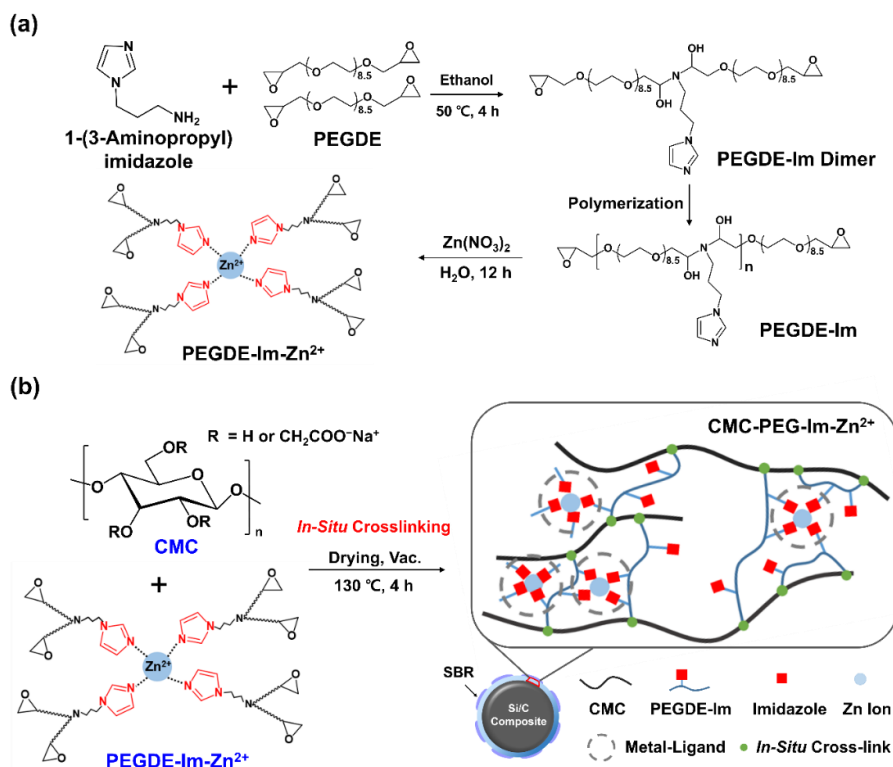


Figure 2.1. (a) Synthetic scheme for the preparation of the metal-ligand complex **PEGDGE-Im-Zn²⁺**. (b) Graphical illustration of the supramolecular network on the Si/C composite formed by *in situ* crosslinking between CMC and **PEGDGE-Im-Zn²⁺**.

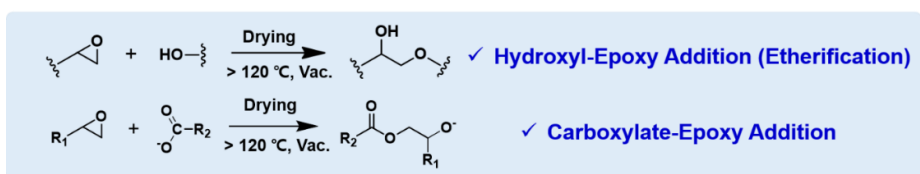
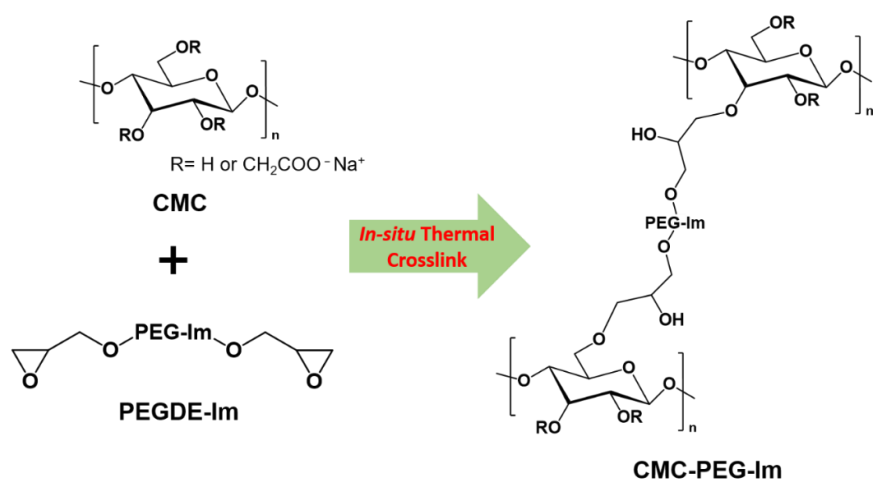


Figure 2.2. Scheme of the chemical reaction between the hydroxyl and carboxylate groups of CMC and the epoxy group of **PEGDGE-Im**.

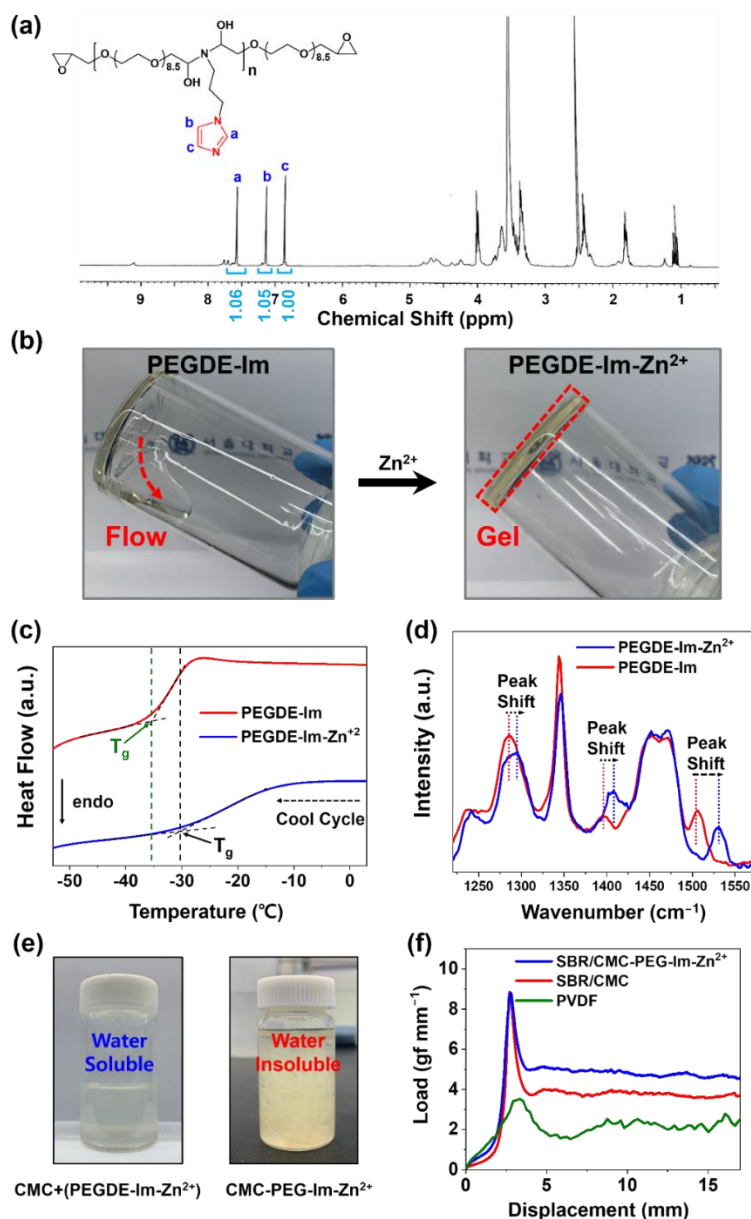


Figure 2.3. (a) ^1H NMR spectrum of PEGDGE-Im ($\text{DMSO-}d_6$, 400 MHz). (b) Digital photographs of (left) PEGDGE-Im and (right) PEGDGE-Im- Zn^{2+} . (c) Differential scanning calorimetry (DSC) profiles and (d) Raman spectra of PEGDGE-Im and PEGDGE-Im- Zn^{2+} . (e) Solubility test of CMC+(PEGDGE-Im- Zn^{2+}) in water before (left) and after (right) *in situ*

crosslinking. (f) Results of the 180° peeling test of the Si/C electrodes with different binders.

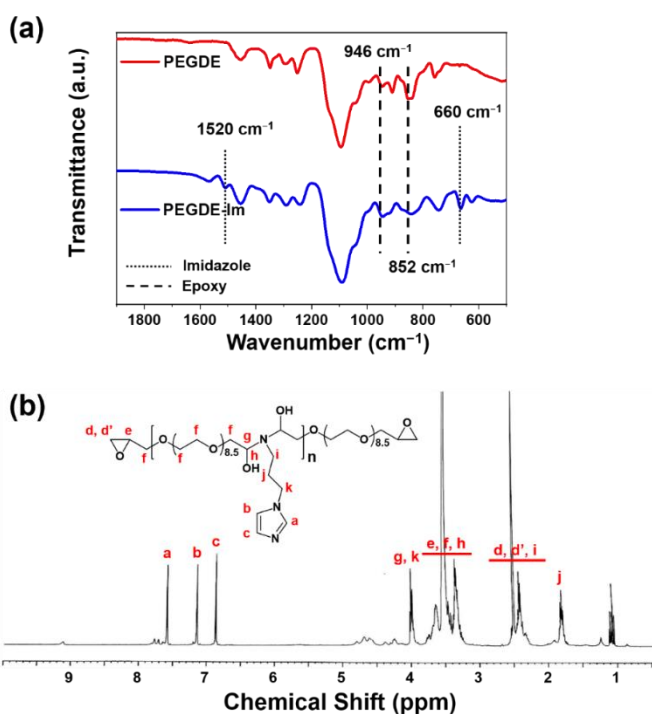


Figure 2.4. (a) FT-IR profiles of PEGDGE and **PEGDGE-Im**. (b) ^1H NMR spectrum of **PEGDGE-Im**.

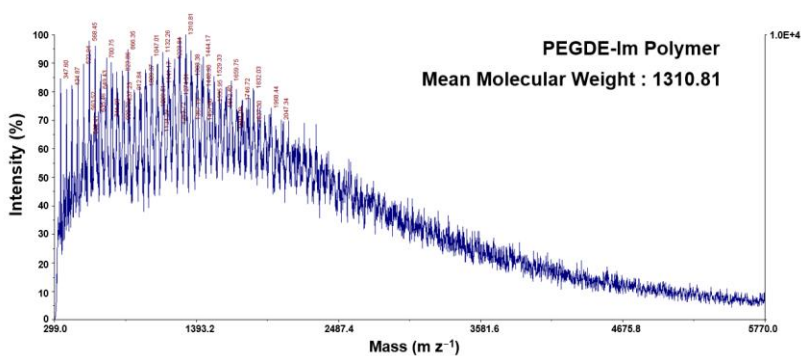


Figure 2.5. Molecular weight distribution and mean value of **PEGDGE-Im**.

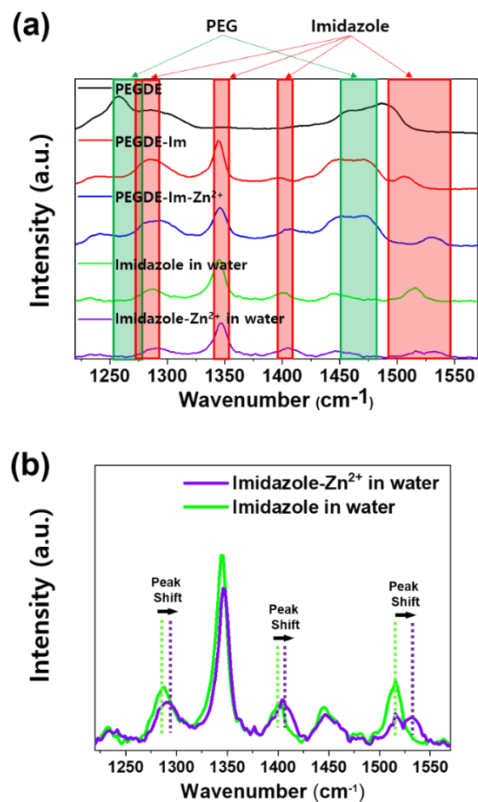


Figure 2.6. Raman spectra showing (a) PEG and imidazole in **PEGDGE-Im** and **PEGDGE-Im-Zn²⁺** and (b) imidazole and imidazole-Zn²⁺ in water.

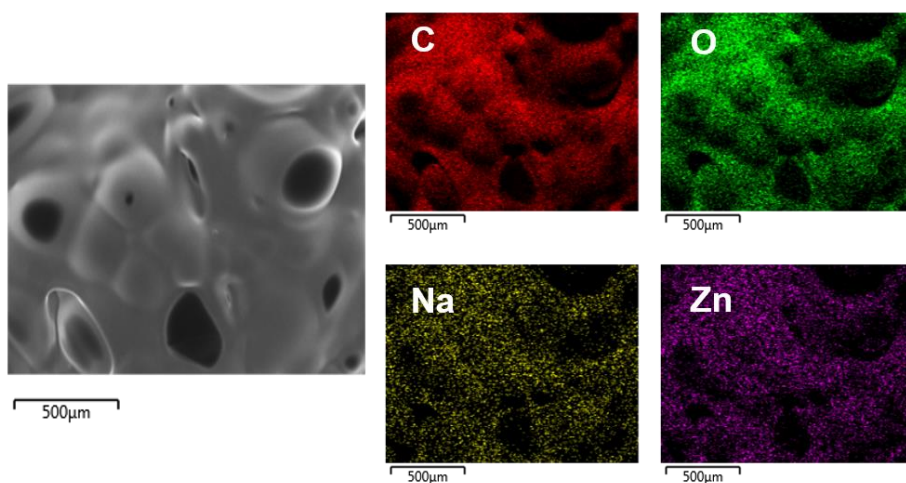


Figure 2.7. SEM image and corresponding elemental mapping of **PEGDGE-Im-Zn²⁺** using EDS.

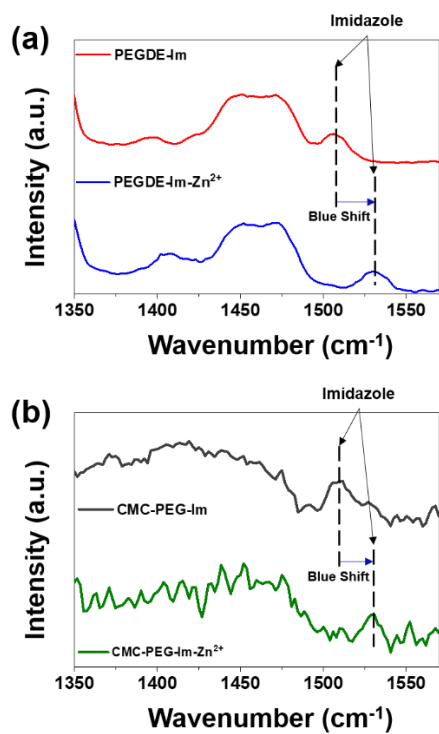


Figure 2.8. Raman spectra of (a) **PEGDGE-Im** and **PEGDGE-Im-Zn²⁺** and (b) **CMC-PEG-Im** and **CMC-PEG-Im-Zn²⁺**.

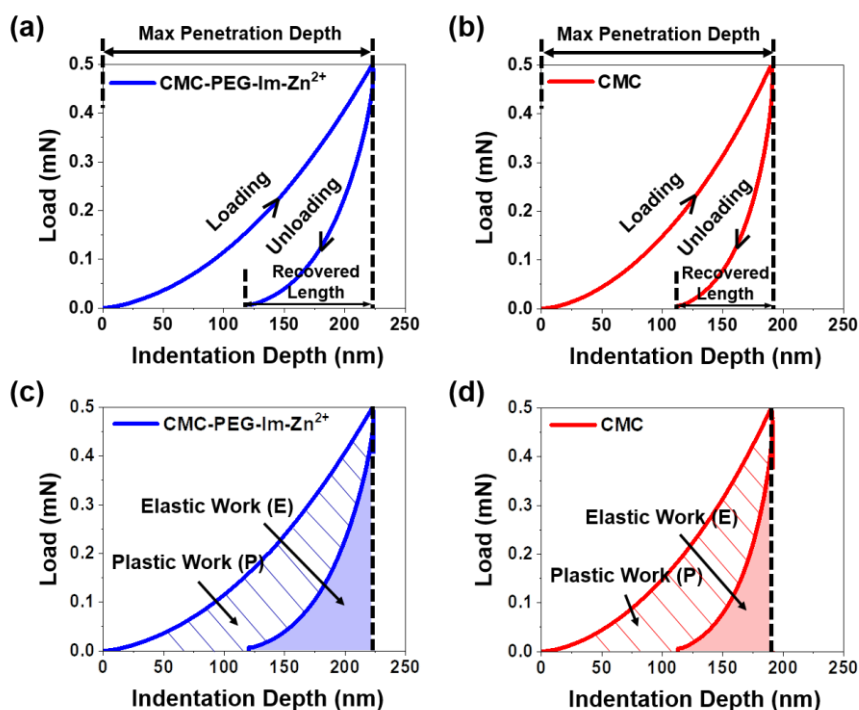


Figure 2.9. Nanoindentation results of **CMC-PEG-Im-Zn²⁺** (blue) and CMC (red). Load-displacement curves of the (a) **CMC-PEG-Im-Zn²⁺** and (b) CMC films during a loading-unloading cycle. Maximum penetration depths and recovered lengths are denoted along the x-axes. Load-displacement curves of the (c) **CMC-PEG-Im-Zn²⁺** and (d) CMC films during the same loading-unloading cycle with plastic work (P) and elastic work (E) noted as areas underneath the curves.

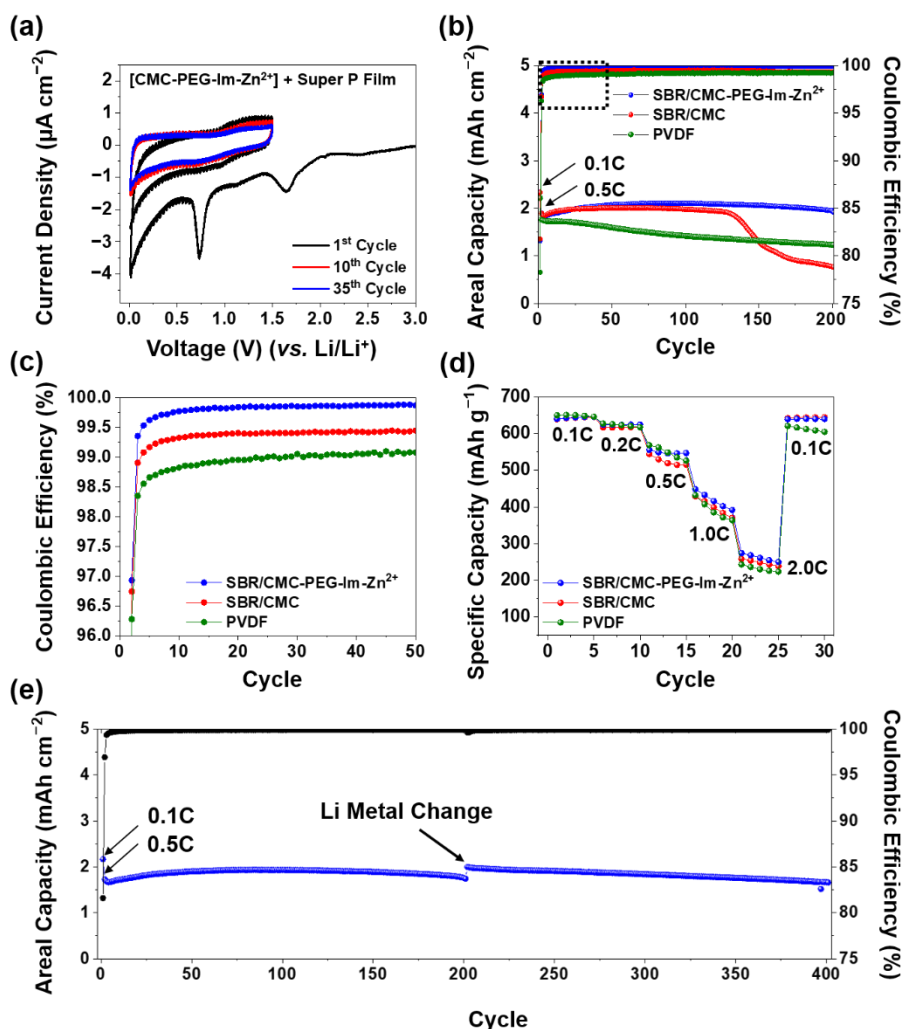


Figure 2.10. Electrochemical test results of half-cells using SBR/CMC, SBR/CMC-PEG-Im-Zn²⁺, and PVDF binders. (a) CV profiles of CMC-PEG-Im-Zn²⁺ with Super P (1:1 wt%) at 0.05 mV s⁻¹ in the potential range of 0.01–1.5 V vs. Li/Li⁺. (b) Cycling performance of Si/C electrodes using PVDF (green), SBR/CMC (red), and SBR/CMC-PEG-Im-Zn²⁺ (blue) measured at 0.5C. (c) Corresponding Coulombic efficiencies in the cycle range of 1–50. (d) Rate capability at various C-rates. (e) Long-term cycling performance of the Si/C electrode containing SBR/CMC-PEG-Im-Zn²⁺ binder when measured at 0.5C (1.17 mA cm⁻²).

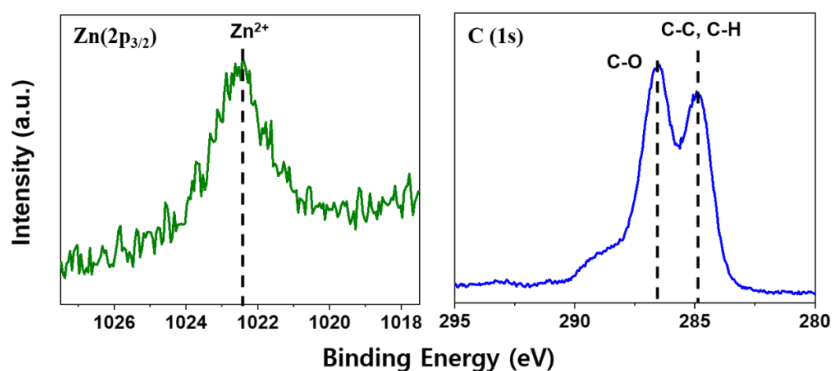


Figure 2.11. XPS results of the **CMC-PEG-Im-Zn²⁺** film after 30 CV cycles at 0.5 mV s^{-1} in the voltage range of 0.01–1.5 V.

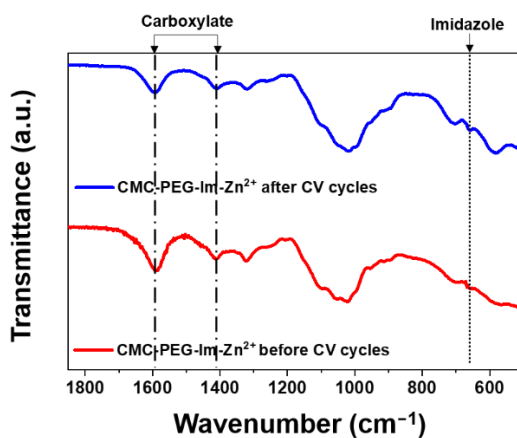


Figure 2.12. FT-IR spectra of the **CMC-PEG-Im-Zn²⁺** film before and after 30 CV cycles at 0.5 mV s^{-1} in the voltage range of 0.01–1.5 V.

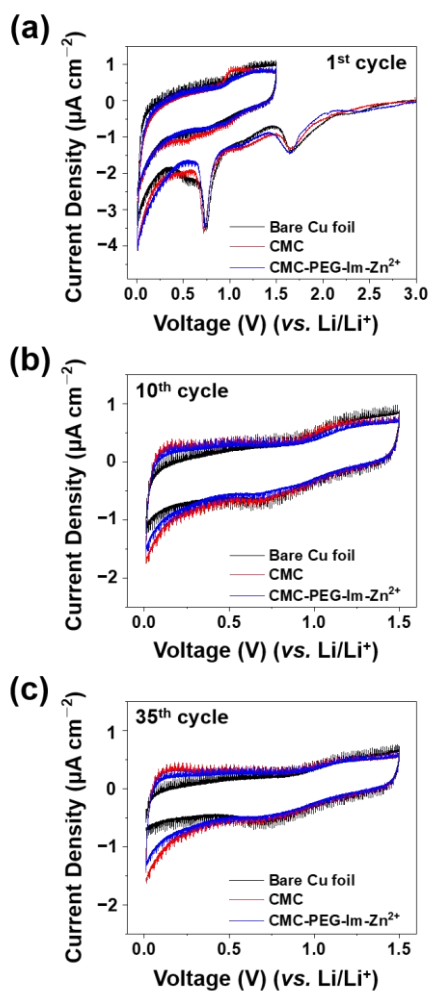


Figure 2.13. CV profiles of CMC, CMC-PEG-Im- Zn^{2+} with Super P (1:1 wt%), and bare Cu foil at the (a) 1st cycle, (b) 10th cycle, and (c) 35th cycle.

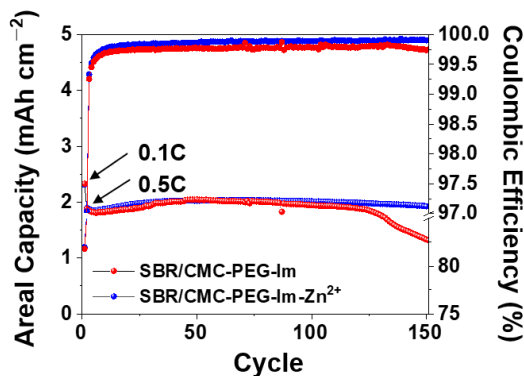


Figure 2.14. Cycling performance of the Si/C electrodes containing SBR/CMC-PEG-Im and SBR/CMC-PEG-Im- Zn^{2+} .

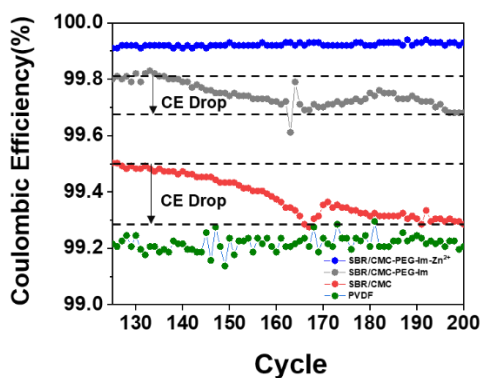


Figure 2.15. Coulombic efficiencies of the Si/C electrodes containing PVDF (green), SBR/CMC (red), SBR/CMC-PEG-Im (gray), and SBR/CMC-PEG-Im- Zn^{2+} (blue) in the cycle range of 125–200.

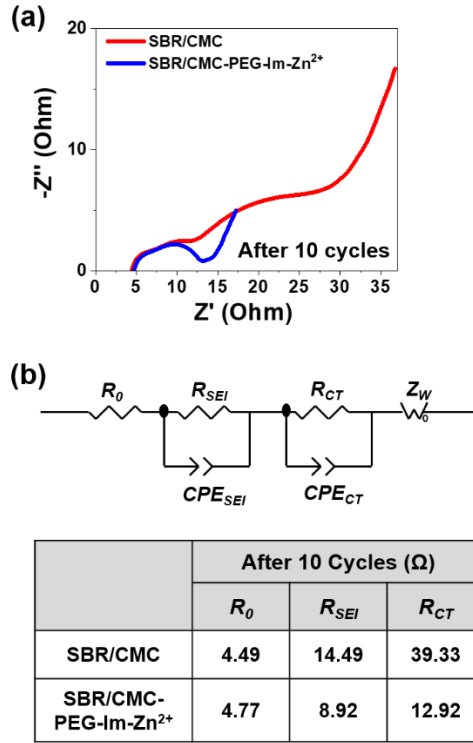


Figure 2.16. (a) EIS fitting of electrodes after 10 cycles at 0.5C. (b) Equivalent circuit for the EIS and corresponding resistance results obtained by fitting to the circuit.

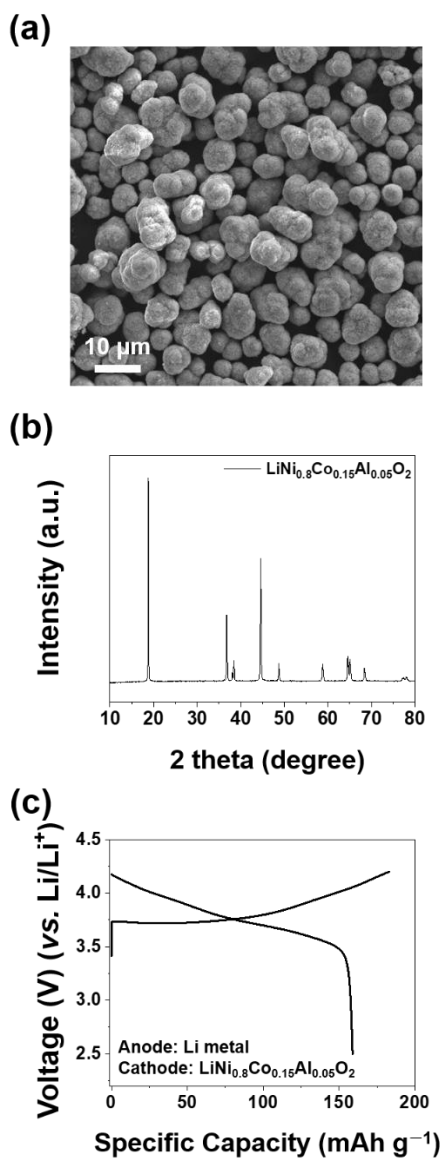


Figure 2.17. (a) SEM image and (b) XRD pattern of NCA powder. (c) 1st charge-discharge profile of NCA under the half-cell configuration when scanned at 0.1C.

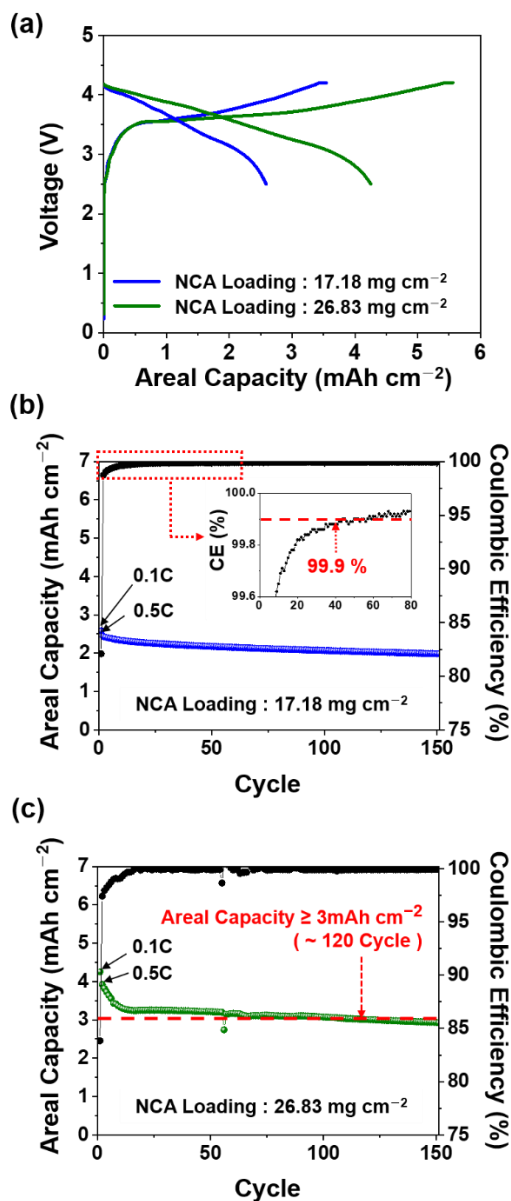


Figure 2.18. Electrochemical performance of the full-cell containing the Si/C electrode with SBR/CMC-PEG-Im-Zn²⁺ binder. (a) Initial charge-discharge profiles of Si/C-LiNi_{0.8}Co_{0.15}Al_{0.05}O₂ (NCA) full-cells with different NCA loadings at 0.1C. Cycling performance of the full-cells at 0.5C along with their Coulombic efficiencies over cycling when the NCA loading is (b) 17.18 and (c) 26.83 mg cm⁻². The n/p ratios of both cells are 1.1.

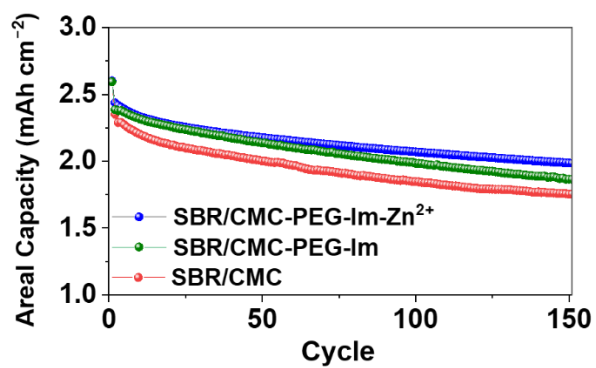


Figure 2.19. Cycling performance of the full-cells based on the SBR/CMC-PEG-Im-Zn²⁺, SBR/CMC-PEG-Im, and SBR/CMC binders.

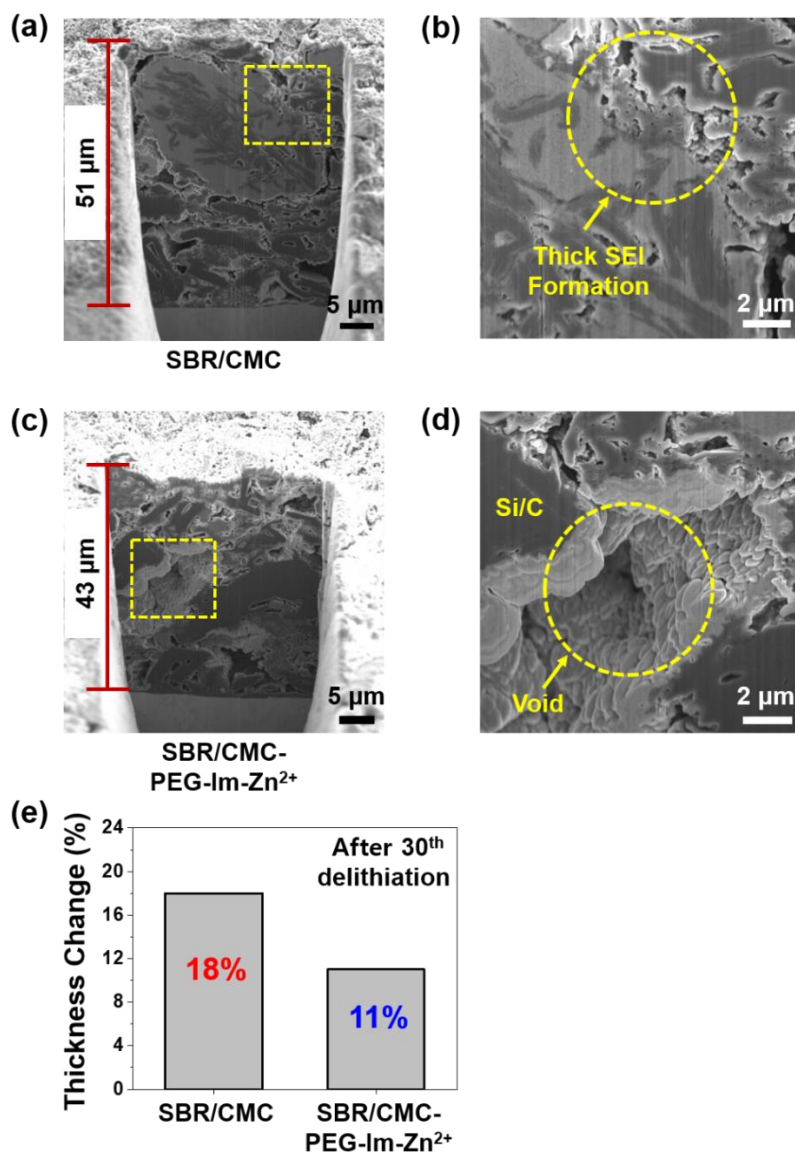


Figure 2.20. Cross-sectional SEM images of Si/C electrodes. (a) Si/C-SBR/CMC electrode after the 30th delithiation and (b) a magnification of the area within the yellow box. (c) Si/C-SBR/CMC-PEG-Im-Zn²⁺ electrode after the 30th delithiation and (d) a magnification of the area enclosed by the yellow box. (e) Thickness changes of the Si/C electrodes after the 30th delithiation.

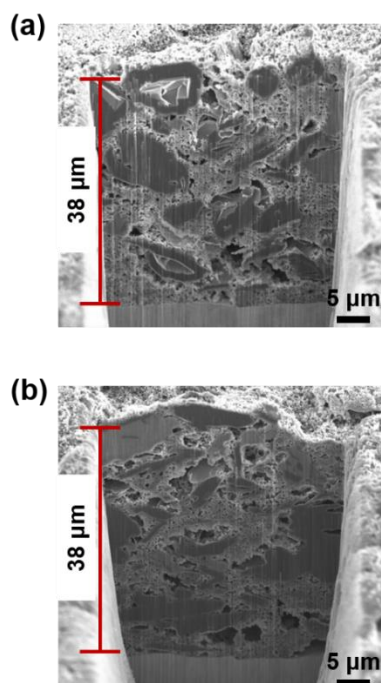


Figure 2.21. Cross-sectional SEM images of the (a) Si/C-SBR/CMC and (b) Si/C-SBR/CMC-PEG-Im-Zn²⁺ electrodes in the pristine state. The thicknesses of both electrodes were 38 μm.

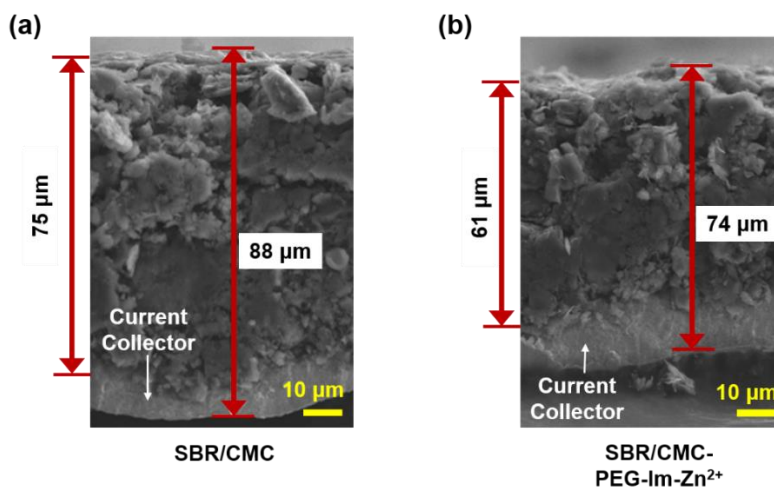


Figure 2.22. Cross-sectional SEM images of the (a) Si/C-SBR/CMC and (b) Si/C-SBR/CMC-PEG-Im-Zn²⁺ electrodes after the 135th delithiation.

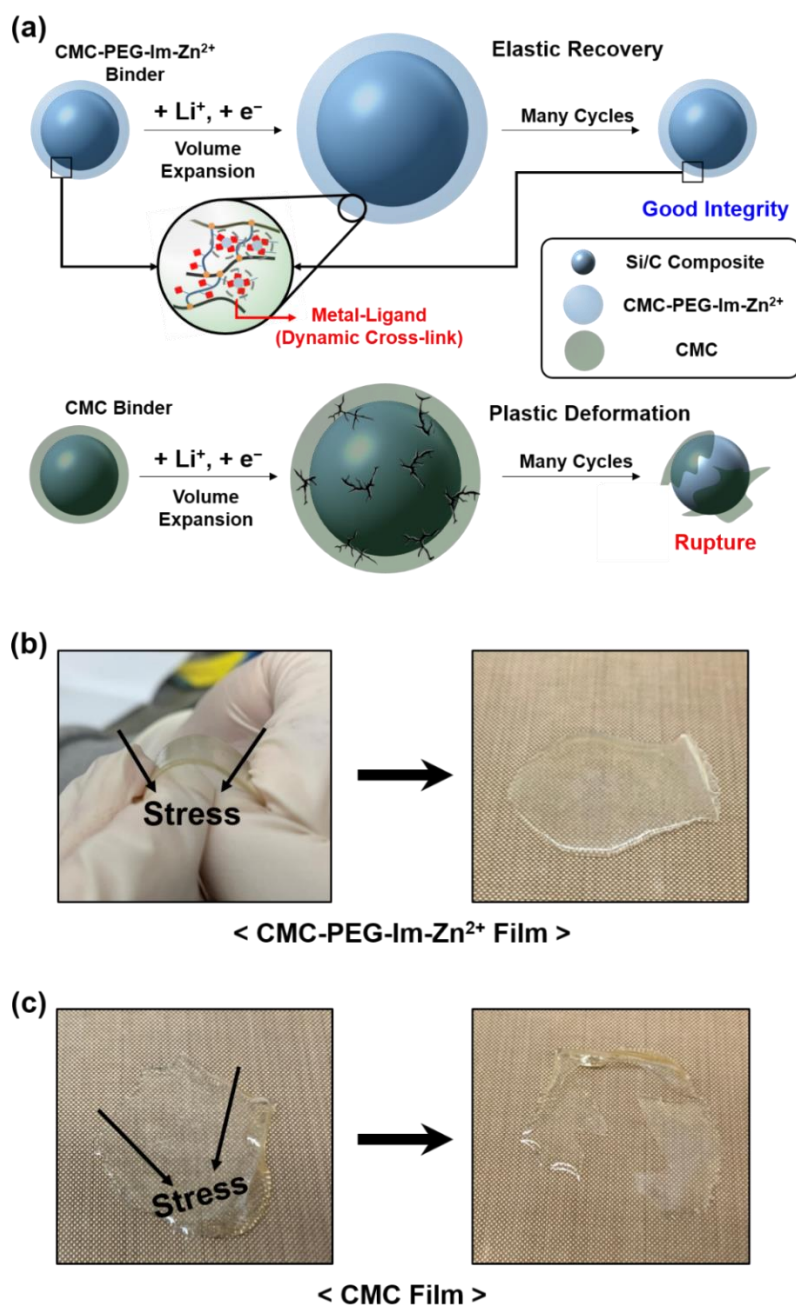


Figure 2.23. (a) Proposed operating mechanisms of the binders in the electrodes during lithiation and delithiation. (b and c) Photographs of the **CMC-PEG-Im-Zn²⁺** and CMC films before (left) and after (right) two times of bending-unbending action.

Chapter 3. Multi-Functioning Separator for High-Performance Lithium-Metal Batteries

3.1 Introduction

The advances of rechargeable battery system facilitate the commercializing and popularizing of drones, portable devices, and electric vehicles (EVs).^[1] In regard to these rechargeable batteries, a variety of research has led to obvious consensus that lithium (Li) metal plays a significant role in the enhancing of energy density owing to their high theoretical capacity (3860 mAh g⁻¹) and low thermodynamic redox potential (-3.04 V vs. standard hydrogen electrode).^[2] Nevertheless, battery community is still struggling with several failure mechanisms of Li metal anode during repeated charge-discharge cycles.^[3] These failure mechanisms include immense volume expansion and rampant formation of Li dendrite which originate destabilization of the solid-electrolyte-interphase (SEI) layer, electrolyte exhaustion and electrically insulated dead Li.^[4]

To realize high-energy and high-performance LMBs, various studies have been conducted considering fundamental factors to minimize the side effects of Li metal. Undoubtedly, the unstable SEI layer is a critical factor for stabilizing the interface of Li metal anode. The well-formed SEI layer composed of inorganic and organic parts is essential for selective Li ion diffusion and thermodynamic stability between Li metal and electrolyte.^[8] However, the insecure SEI layer provokes constant parasitic reactions, which eventually lead to rapid battery failure.^[9] To overcome the weakness of the SEI

layer derived from the general liquid electrolyte, especially solvents, considerable strategies in the SEI layer engineering have been suggested to operate high-performance Li metal anode such as modifying the composition of the SEI layer.^[10] The inorganic compounds containing lithium nitrate (LiNO_3) and lithium fluoride (LiF) are well-known for having high interfacial energy compared to organic compounds.^[11] Particularly, LiF has been regarded as a desirable element of SEI layer due to its unique properties of wide electrochemical potential window,^[12] low calculated barriers to Li ion diffusion,^[13] and high mechanical strength,^[14] significantly contributing to homogeneous Li ion deposition and alleviation of dendritic Li growth.

Generally, LiF is mainly derived by decomposition of electrolyte components such as salt anion and F-containing additives. However, inhomogeneous and unstable SEI layer is accumulated from the indiscriminate decomposition of the electrolyte. Unorganized SEI layer on the Li metal surface lowers interfacial stability, eventually accelerating dendritic Li growth by unbalanced charge distribution and nonuniform Li ion flux. Therefore, the strategy of constructing an artificial SEI layer with F-source has advantage in that uniform LiF layer can be induced pre-emptively. Along this line, we focused on a separator coating with synergetic combination of the inorganic part which can supply F-species in the inner SEI layer and the organic part endowing elasticity to withstand volume fluctuation. Specifically, graphene oxide with fluorination (**GO-F**) as the inorganic component and the organic part composed of polyacrylic acid (PAA)-based polymer was introduced to the coating layer on the PP separator. F-functional group in **GO-F** could be a precursor to induce F-enriched SEI layer, and high mechanical strength of **GO-F** could restrict perpendicular growth of Li dendrite.^[15] Viscoelastic property of PAA could effectively buffer immense volume expansion of Li metal and reduce side reactions resulting therefrom.^[16] These two materials formed

covalent bond by thermal treatment using poly(ethylene glycol) diglycidyl ether (PEGDGE) to develop solid system of the organic/inorganic crosslinked network on the separator (**OICNS**). Figure 3.1a illustrates the formation of dendrites during cycling and entailed unsound SEI layer in the absence of the coating layer on the separator. In contrast, as illustrated in Figure 3.1b, homogeneous Li plating/stripping can be accomplished when the **OICNS** is employed on Li metal surface. As a result, full-cells paired with LiFePO₄ (LFP) could be operated with improved performance. This study proves that the synergetic integration of the crosslinked organic/inorganic composites to the PP separator, which induces F-enriched interface, enhances stability of Li metal anode, and thus provides the possibility of one step closer to the requirements of the industry on Li metal anode.

3.2 Experimental section

Materials and Chemicals. Poly(vinylidene fluoride) (PVdF) (M_w=534k), LiNO₃, lithium bis(trifluoromethane) sulfonimide (LiTFSI), 1,2-dimethoxyethane (DME), 1,3-dioxolane (DOL), lithium hydroxide (LiOH), PAA (M_w=450k), PEGDGE (M_n=500), diethyl ether, potassium permanganate (KMnO₄), hydrochloric acid (HCl), hydrofluoric acid (HF), phosphoric acid (H₃PO₄), sulfuric acid (H₂SO₄), and ethanol were purchased from Sigma Aldrich (USA). N-methyl-2-pyrrolidone (NMP) for solvent was purchased from Junsei (Japan). For conductive agent, Super P was purchased from Timcal (Switzerland). PP separator and LFP were purchased from Welcos (South Korea).

Synthesis of Inorganic Compound. GO-F was synthesized using

improved Hummer's method with some modifications. 1 g of graphite was stirred with solution of 90 ml of H_2SO_4 10 ml of H_3PO_4 , and 10 ml of HF at 60 °C for 3 hours. And then, 4 g of KMnO_4 was poured to graphite dispersion, and then the mixture was stirred consistently for another 12 hours at the same temperature. After the solution cooled down to 20 °C, 3 ml of hydroperoxide (H_2O_2) and ice were sequentially poured until the color changed from black to yellowish brown. The mixture including **GO-F** was gradually washed with HCl, ethanol, water and diethyl ether using centrifuge. At last, yellowish-brown **GO-F** powder was acquired after drying under vacuum condition at room temperature to eliminate residual solvent.

Synthesis of Organic Compound. 1 g of PAA and 0.5 g of LiOH were solved in 100 ml of water for substitution of lithium on PAA. After complete dissolution, 100 mg of PEGDGE was added into the solution and then stirred for an hour at 60 °C. Next, the solution was dialyzed for a day using a dialysis membrane to eliminate impurities and unreacted matters, and then lyophilization was carried out for a week. Finally, **PAA-PEGDGE** powder was acquired.

Characterizations of Materials. The exfoliation of graphite and fluorination were measured using XRD (Smart lab, Rigaku, Japan) in the 2θ range of 5° to 65°. The XPS (Axis-His, Kratos, UK) was conducted using sputtering method after etching samples for 10 seconds (10kV). The ratio of covalent C-F bond and semi-ionic C-F bond, and relative contents of the SEI layer components were characterized. FT-IR (TENSOR 27, Bruker, Germany) and ^1H NMR (Avance III, Bruker, Germany) were carried out to analyse the

chemical structures of materials. The T_g of the polymers were estimated using DSC (DSC 400, PerkinElmer, USA) at ramping rate of $10\text{ }^{\circ}\text{C min}^{-1}$. And the TGA was performed in the range from 100 to 1000 $^{\circ}\text{C}$, at a ramping rate of $10\text{ }^{\circ}\text{C min}^{-1}$. EDS mapping was conducted to visualize elemental distribution of materials. Contact angle measurements (DSA100, Kruss, Germany) were carried out by dropping water onto the membrane surface. The morphological analyzation of Li metal surface was conducted using SEM (JSM-7800F Prime, JEOL, Japan). Cross-sectional images of Li metal anode were analyzed using FIB (Helios G4, Thermo Fisher Scientific, USA).

Preparation of Electrode. The cathodes for full-cells were fabricated containing LFP, PVdF, and Super P in a weight ratio of 90 : 5 : 5. In this process, PVdF was first dissolved in NMP. The slurry based on NMP was cast on aluminum foil using blading, then the electrodes are dried under vacuum at 60 $^{\circ}\text{C}$.

Electrochemical measurement. All electrochemical performance was evaluated in CR2032 type coin cells assembled in an argon-filled glove box. Polypropylene membrane (Celgard 3501) was utilized as a separator and the ether-based electrolyte, 1 M LiTFSI and 0.2 M LiNO_3 in DOL/DME (1/1 volume ratio), was used for all the cells. Battery cycler (WBCS 3000, WonATech, South Korea) was operated at 25 $^{\circ}\text{C}$ and all cells had resting time for 6 h. The Li symmetric cells were composed of Li metal foil (Honjo Metal, Japan) with a thickness of 300 μm and the coating layer on the PP separator was employed on both sides of the Li metal electrode. For consistency, the control cell was also assembled with two PP separators. The loading of LFP

was 10.0 mg cm^{-2} , paired with $40 \text{ }\mu\text{m}$ Li metal foil. The full-cell tests were performed in the potential range of 2.5–4.0 V in constant current (CC) mode. EIS tests were conducted with symmetric cells after cycling, utilizing a potentiostat (VSP, Biologic).

3.3 Result and discussion

For an inorganic part of the coating layer on the separator, **GO-F** was synthesized from graphite precursor by using the improved Hummers' method with modifications.^[17] To confirm oxidation and formation of C-F bond of the acquired **GO-F**, X-ray diffraction (XRD) analysis was carried out (Figure 3.2). In contrast to appearance of a characteristic (002) peak at 26.5° in graphite, the graphitic peak disappeared in **GO-F**.^[18] Instead, a characteristic peak at 10.40° almost similar to that of GO ($2\theta=10.74^\circ$) was observed, which means oxidization and exfoliation of the graphite.^[19] The transition from graphite to GO can also be captured through the color change from dark gray to yellowish powder.^[19a] The slight peak shift of **GO-F** to lower side can be explained by the strengthened repulsive effect owing to the fluorination.^[17a] Moreover, the formation of the C-F bond was identified by Fourier-transform infrared (FT-IR) spectroscopy as well, exhibiting a peak at 1080 cm^{-1} that is associated with the C-F bond (Figure 3.3).^[17a] To define F-species of **GO-F** in detail, X-ray photoelectron spectroscopy (XPS) was examined, and its profile is shown in Figure 3.4 and Figure 3.5. Two kinds of peaks appeared in its F 1s spectra, where the peak at 688.3 eV corresponds to the covalent C-F bond and the peak at 687.3 eV is attributed to the semi-ionic C-F bond, especially CF_3 .^[17a, 20]

For the organic part of the coating layer, **PAA-PEGDGE** was synthesized. To this end, lithium hydroxide was reacted with the carboxylic acid

of PAA to make lithium substituted-PAA (LiPAA), prior to subsequent linkage with PEGDGE to form **PAA-PEGDGE** through carboxylate-epoxy addition reaction. The FT-IR spectra of LiPAA exhibited asymmetric and symmetric carboxylate characteristic peaks at 1552 cm^{-1} and 1409 cm^{-1} respectively, which are different from acid peak of PAA at 1700 cm^{-1} (Figure 3.6).^[21] The chemical reaction between PEGDGE and LiPAA was proved by ^1H nuclear magnetic resonance (NMR) spectrum of the **PAA-PEGDGE** (Figure 3.7). When the polymer was dissolved in deuterium oxide (D_2O), chemical shifts of hydrogens on epoxy groups were found at 2.89 ppm and 2.98 ppm, indicating that epoxy groups were still left to further reaction with **GO-F**.^[22] The FT-IR spectra of **PAA-PEGDGE** showed the aforementioned peaks of LiPAA along with peaks at 946 cm^{-1} and 1096 cm^{-1} that are the characteristic peaks of epoxy groups,^[23] also identifying the successfully connected structure and the presence of epoxy groups in **PAA-PEGDGE** (Figure 3.8). Meanwhile, not only PEGDGE was branched to PAALi but also acted as a crosslinker for the connection of PAALi mainchains. To verify the crosslinked form of **PAA-PEGDGE**, differential scanning calorimetry (DSC) of PAA and **PAA-PEGDGE** was carried out and the resultant glass transition temperature (T_g) of the polymers were displayed in Figure 3.9. **PAA-PEGDGE** exhibited increased T_g ($137\text{ }^\circ\text{C}$) than that of PAA ($127\text{ }^\circ\text{C}$), which is originated from lowered chain mobility owing to bridging between the epoxy groups of a PEGDGE chain and LiPAA.^[24] This crosslinking aspect of **PAA-PEGDGE** was also verified by thermogravimetric analysis (TGA) (Figure 3.10). Thermal degradation profiles represented that the thermal stability of **PAA-PEGDGE** was highly strengthened after linkage of polymers, because the crosslinked polymer network restrains the mobility and rotation itself.^[25] Although **PAA-PEGDGE** had the partially crosslinked system, epoxy groups which are indispensable for their further crosslinking to **GO-F** were still observed through the above NMR and FT-IR results (Figure 3.7 and Figure 3.8).

Although each organic and inorganic material could individually play the aforementioned significant roles on Li metal surface, **GO-F** was not able to be coated solely on the separator independently without the cooperation of the polymeric component (Figure 3.11b). To construct a synergistically robust combination between organic and inorganic components, the hydroxyl groups in **GO-F** and the epoxy groups in **PAA-PEGDGE** were reacted *via* thermal treatment under vacuum condition, after filtration of the blend of both materials for a coating layer on the separator (Figure 3.12).^[26] Before the crosslinking, a simple mixture of **GO-F** and PEGDGE had liquidity when the vial was held upside down, whereas a gelated phase was displayed after heat treatment under vacuum condition. In addition, the formation of the **OICNS** *via* crosslinking was checked by the color change of the coating layer on the separator. To elucidate the role of PEGDGE for crosslinking, **PAA+GO-F** layer without crosslinked network was fabricated. Even under the same thermal drying process, **PAA+GO-F** layer exhibited yellowish-brown color (Figure 3.11a), whereas that of the **OICNS** was dark brown (Figure 3.12). This can be explained by the increase of C/O ratio owing to the reduction of oxygen-containing functional groups during the epoxy-to-hydroxyl reaction.^[26a] Figure 3.12 shows digital photograph and SEM-EDS images to exhibit homogeneity of the **OICNS** at the bulk-scale and micro-scale, respectively. Through SEM-EDS, uniformly scattered **GO-F** particles throughout the **OICNS** were identified, contributing to the formation of homogeneous LiF-rich SEI layer.

To check the effectiveness of the **OICNS** for stabilizing Li metal interface, Li symmetric cells were assembled and evaluated. Figure 3.13a displays the repeated plating/stripping profiles of Li symmetric cells with the PP separator and the **OICNS** when cycled at a current density of 1 mA cm^{-2} with capacity of 1 mAh cm^{-2} . The cell fabricated with the **OICNS** maintained stable voltage profile over 1000 h with a low overpotential of 25 mV (Figure

3.13a and b), which indicated the ability of the **OICNS** for Li metal anodes. On the other hand, the overpotential of the bare cell was gradually increased over time, which meant growing interfacial resistance originated from fragile and unsound SEI layer arousing formation of dendrite and accordingly intensifying parasitic reactions on the interface between electrolyte and Li metal. Remarkably, the unstable voltage curve with fluctuation was also observed in the cell with PAA+**GO-F** layer after 500 h, thus proving the role of crosslinking between organic and inorganic materials using PEGDGE for the robust coating layer (Figure 3.14). This electrochemical distinction demonstrated the effect of the **OICNS** on Li metal anodes by restraining the reconstruction of SEI layer through the formation of chemically and mechanically stable interface in advance with synergetic combination of organic and inorganic components. To examine the interfacial stability of Li metal anodes with the **OICNS** on cycling, electrochemical impedance spectroscopy (EIS) was performed on Li symmetric cells with and without the coating layer after 1st, 5th, 20th, and 50th cycle. After 1st cycle, the bare Li electrode showed a total resistance (R_{total}) of $\sim 173\ \Omega$ from the charge transfer resistance (R_{CT}) and SEI layer resistance (R_{SEI}) at the interface (Figure 3.15a).^[27] The R_{total} value rarely decreased until 5th cycle and gradually reduced after several cycle numbers to confirm the slow stabilization of the SEI layer, which is structurally loose and poorly conductive leading to continuous electrolyte consumption. In Contrast, the R_{total} value of the Li symmetric cell with the **OICNS** was $\sim 91\ \Omega$ after 1st cycle and finally reached $\sim 14\ \Omega$ after the 50th cycle (Figure 3.15b). The R_{total} values were markedly smaller than those of the bare Li electrodes in every cycle and decreased in succession as the cycle number increased, which also demonstrated the early formation of stable interface with well-functioning and highly tolerant SEI layers within 5 cycles. This observation was consistent with the low overpotential of the Li anodes with the **OICNS**, thus it was confirmed that this

OICNS can induce well-formed interface from chemical modification of SEI layer to effectively deliver Li ions across the interface and prevent additional parasitic side reactions.

To investigate the components of the SEI layer, XPS was conducted according to the depth of the SEI layer. The generation of F-rich SEI layer, especially LiF component, was evidenced by the comparison of F 1s XPS depth profiles of Li anodes with and without the **OICNS** (Figure 3.19a and 3.16b). These analyses were performed after 5 cycles of Li plating and stripping with a capacity of 1 mAh cm⁻² at 0.5 mA cm⁻². The peaks observed at 688.4, 687.2, and 685 eV can be assigned to the CF₃ bond, C-F bond, and LiF, respectively.^[28] The peak of CF₃ bond represents the TFSI anion, and the broad shoulder peak of the C-F bond arises from the transient components during breakdown of the CF₃ bond.^[28] The peak of LiF can be attributed to the reaction between the **GO-F** and Li metal as well as further decomposition of the TFSI anion. Based on this information, the continuous appearance of the C-F bond peak with subsequent sputtering up to 180 s indicated that the F-species of the SEI layer on the unprotected Li metal electrode was the product of electrolyte decomposition (Figure 3.16c). Whereas in the case of the SEI layer on the Li metal electrode with the **OICNS**, there was no C-F bond peak in every depth profile with different sputtering time and the CF₃ bond peak vanished promptly after the full removal of the residual **OICNS** (Figure 3.16d). In addition, from the continuous appearance of LiF as the only species, it could be interpreted that the LiF was generated by the reaction between the **GO-F** in the coating layer and Li metal, not by the decomposition of the electrolyte. These XPS results demonstrating that the uniform and sufficient LiF component in the inner SEI layer was derived preferentially from the decomposition of the **GO-F**, finally contributing to improved interfacial kinetics by the well-formed F-rich SEI layer.

To prove the capability of the **OICNS** in practical Li metal batteries, the full-cell evaluations were conducted by pairing the LFP cathode with Li anode. The cyclic performance of full-cells was tested at 0.5C except for the first cycle (0.1C). For the LFP cathode with active material loading of 10.0 mg cm⁻² and thin 40 μm Li metal foil, the full-cell with the **OICNS** displayed superior cycling performance with a highly reversible capacity and exhibited a capacity retention of 98% after 250 cycles, with the average CE of 99.8% (Figure 3.17a and b). On the other hand, the full-cell with the pristine PP separator suddenly decayed near 238 cycles with the average CE of 99.6%. These results verified the stable SEI layer formed on Li anode was retained effectively without collapse even after long cycling. Figure 3.17c displays the rate performance of the LFP-Li metal full-cells, when the current densities of 0.1C, 0.2C, 0.5C, 1C, and 0.1C to confirm the recovery rate were applied for every three cycles. Both cells exhibited similar discharge capacity of 160 mAh g⁻¹ at 0.1C. However, as the current density increased, the capacity gap between the two distinct cells gradually increased, leaving only 110 mAh g⁻¹ at 2C in the full-cell with the PP separator. Otherwise, the full-cell with the **OICNS** showed excellent rate capability of nearly 158, 154, 152, 146, and 135 mAh g⁻¹ at the current density from 0.1C to 2C, verifying the enhanced interfacial kinetics by the introduction of the **OICNS**. This superior rate capability was attributed to decreased resistance with respect to ionic conductivity by introducing the **OICNS**, in accordance with the results of EIS in figure 3.15a and b. When the current density was recovered to 0.1C, the full-cell with the **OICNS** can still deliver 157 mAh g⁻¹, which preserved 99.6% of the initial capacity at 0.1C.

To examine the superiority of the Li metal anodes with the **OICNS** visually, cross-sectional SEM was conducted to identify the thickness and morphology of the Li metal electrode after the 20th discharge. Highly porous Li

dendrites with a thickness of 15 μm were observed on the pristine Li anode, identifying lower reversibility of Li plating/stripping due to the unstable interface formed by uncontrollable parasitic reactions (Figure 3.18a). In stark contrast, the robust network of the **OICNS** can alleviate the Li ion concentration gradient through homogeneous and rapid interfacial charge transfer and maintain the stabilized interface firmly, leading to dendrite-free and compact Li deposits with a thickness of 6 μm (Figure 3.18b). Also, as shown in top-viewed SEM images of Li metal electrodes after 20th cycles in Li symmetric cells (Figure 3.19 and 3.20), similar tendency was observed. Whereas the smaller size of Li dendrites with highly exposed surface area was observed in the Li deposits with the PP separator (Figure 3.19), the Li deposits using the **IOCPL** displayed large chunk of Li with smooth surface (Figure 3.20). The difference in the morphology of cycled Li electrodes was attributed to interfacial kinetics derived from the protective layer, together with the mechanical strength of **GO-F**.

3.4 Conclusion

In summary, we demonstrated the **OICNS** to stabilize LMA with its synergistic combination of organic PAA and inorganic **GO-F**. The robust network through crosslinking and mechanical superiority including high mechanical strength of **GO-F** and viscoelastic property of PAA contribute to restricting dendritic Li growth and withstand the enormous volume expansion of the Li metal to maintain a stable interface without destruction. Moreover, the F-rich inner SEI layer induced by **GO-F** and polar functional groups enable homogeneous Li plating *via* facilitated charge transfer kinetics. Through mechanically and chemically well-modified SEI layer, LFP full-cells achieve a

noticeable cyclic and rate performance with uniform Li deposition. This study highlights the significance of a multifunctional coating layer with the synergistic combination of organic and inorganic components as a useful design for stabilizing LMA to realize high-performance lithium metal batteries.

3.5 References

- [1] Y. Liang, C. -Z. Zhao, H. Yuan, Y. Chen, W. Zhang, J-Q. Huang, D. Yu, Y. Liu, M. -M. Titirici, Y. -L. Chueh, H. Yu, Q. Zhang, *InfoMat*, **2019**, *1*, 6.
- [2] a) J. W. Choi, D. Aurbach, *Nat. Rev. Mater.*, **2016**, *1*, 1; b) B. Liu, J. -G. Zhang, W. Xu, *Joule*, **2018**, *2*, 833.
- [3] a) P. G. Bruce, S. A. Freunberger, L. J. Hardwick, J. -M. Tarascon, *Nat. Mater.*, 2012, *11*, 19; b) D. Lin, Y. Liu, Y. Cui, *Nat. Nanotechnol.*, **2017**, *12*, 194.
- [4] a) X. -B. Cheng, R. Zhang, C. -Z. Zhao, Q. Zhang, *Chem. Rev.*, **2017**, *117*, 10403; b) S. Li, M. Jiang, Y. Xie, H. Xu, J. Jia, J. Li, *Adv. Mater.*, **2018**, *30*, 1706375.
- [5] a) Z. A. Ghazi, Z. Sun, C. Sun, F. Qi, B. An, F. Li, H. -M. Cheng, *Small*, **2019**, *15*, 1900687; b) X. Zhang, Y. Yang, Z. Zhou, *Chem. Soc. Rev.*, **2020**, *49*, 3040.
- [6] C. Niu, H. Lee, S. Chen, Q. Li, J. Du, W. Xu, J. -G. Zhang, M. S. Whittingham, J. Xiao, J. Liu, *Nat. Energy*, **2019**, *4*, 551.
- [7] L. S. Kremer, A. Hoffmann, T. Danner, S. Hein, B. Prifling, D. Westhoff, C. Dreer, A. Latz, V. Schmidt, M. W. -Mehrens, *Energy Technol.*,

2020, 8, 1900167.

[8] H. Zhou, S. Yu, H. Liu, P. Liu, *J. Power Sources*, **2020**, 450, 227632;

b) P. Zhai, L. Liu, X. Gu, T. Wang, Y. Gong, *Adv. Energy Mater.*, **2020**, 10, 2001257; c) X. -B. Cheng, R. Zhang, C. -Z. Zhao, F. Wei, J. -G. Zhang, Q. Zhang, *Adv. Sci.*, **2016**, 3, 1500213.

[9] X. Shen, R. Zhang, X. Chen, X. -B. Cheng, X. Li, Q. Zhang, *Adv. Energy Mater.*, **2020**, 10, 1903645.

[10] H. Wu, C. Wang, J. -G. Zhang, W. Xu, *Adv. Energy Mater.*, **2021**, 11, 2003092.

[11] S. Liu, X. Ji, J. Yue, S. Hou, P. Wang, C. Cui, J. Chen, B. Shao, J. Li, F. Han, J. Tu, C. Wang, *J. Am. Chem. Soc.*, **2020**, 142, 2438; b) X. Fan, X. Ji, F. Han, J. Yue, J. Chen, T. Deng, J. Jiang, C. Wang, *Sci. Adv.*, **2018**, 4, 1.

[12] J. Xie, A. D. Sendek, E. D. Cubuk, X. Zhang, Z. Lu, Y. Gong, T. Wu, F. Shi, W. Liu, E. J. Reed, Y. Cui, *ACS Nano*, **2017**, 11, 7019.

[13] a) X. -Q. Zhang, X. Chen, R. Xu, X. -B. Cheng, H. -J. Peng, R. Zhang, J. -Q. Huang, Q. Zhang, *Angew. Chem.*, **2017**, 129, 14395; b) L. Fan, H. L. Zhuang, L. Gao, Y. Lu, L. A. Archer, *J. Mater. Chem. A*, **2017**, 5, 3483.

[14] M. He, R. Guo, G. M. Hobold, H. Gao, B. M. Gallant, *PNAS*, **2020**, 117, 73

[15] J. Bobnar, M. Lozinsek, G. Kapun, C. Njel, R. Dedryvere, B. Genorio, R. Dominko, *Scientific Reports*, **2018**, 8, 5819.

[16] N. -W. Li, Y. Shi, Y. -Xia, Yin, X. -X. Zeng, J. -Y. Li, C. -J. Li, L. -J. Wan, R. Wen, Y. -G. Guo, *Angew. Chem, Int. Ed.*, **2018**, 57, 1505.

[17] a) A, R. Thiruppathi, B. Sidhureddy, W. Keeler, A. Chen, *Electrochem.*

- Commun.* **2017**, 76, 42; b) D. C. Marcano, D. V. Kosynkin, J. M. Berlin, A. Sinitskii, Z. Sun, A. Slesarev, L. B. Alemany, W. Lu, J. M. Tour, *ACS Nano* **2010**, 4, 8, 4806.
- [18] R. Muzyka, M. Kwoka, L. Smedowski, N. Diez, G. Gryglewicz, *New Carbon Materials* **2017**, 32, 1, 15.
- [19] a) M. J. Yoo, H. B. Park, *Carbon* **2019**, 141, 151; b) K. Krishnamoorthy, M. Veerapandian, K. Yun, S. -J. Kim, *Carbon* **2013**, 53, 38.
- [20] W. Feng, P. Long, Y. Feng, Y. Li, *Adv. Sci.* **2016**, 3, 1500413.
- [21] W. Porcher, S. Chazelle, A. Boulineau, N. Mariage, J. P. Alper, T. Van Rompaey, J. -S. Bridel, C. Haon, *J. Electrochem. Soc* **2017**, 164, 14, A3633.
- [22] S. Son, E. Shin, B. -S. Kim, *Macromolecules* **2015**, 48, 600.
- [23] X. Teng, H. Xu, W. Song, J. Shi, J. Xin, W. C. Hiscox, J. Zhang, *ACS Omega* **2017**, 2, 251.
- [24] a) J. Zhang, Z. Huang, D. Liu, *Applied Surf. Sci.* **2017**, 426, 796; b) J. Kim, K. Park, Y. Cho, H. Shin, S. Kim, K. Char, J. W. Choi, *Adv. Sci.* **2021**, 8, 2004290.
- [25] a) S. V. Ebadi, A. Fakhrali, S. O. Ranaei-Siadat, A. A. Gharehaghaji, S. Mazinani, M. Dinarid, J. Haratib, *RSC Adv.* **2015**, 5, 42572; b) P. Chowdhury, A. Hazra, M. K. Mondal, B. Roy, D. Roy, S. P. Bayen, S. Pal, *J. Macromol. Sci. A* **2019**, 56, 773.
- [26] a) B. Shen, W. Zhai, M. Tao, D. Lu, W. Zheng, *Compos. Sci. and Technol.* 2013, 77, 87; [ref 29] b), b) S. Spoljaric, A. Salminen, N. D. Luong, J. Seppala, *RSC Adv.* **2015**, 5, 107992.

- [27] W. Choi, H. -C. Shin, J. M. Kim, J. -Y. Choi, W. -S. Yoon, *J. Electrochem. Sci. Technol.*, **2020**, *11*, 1.
- [28] V. Shutthanandan, M. Nadasiri, J. Zheng, M. H. Engelhard, W. Xu, S. Thevuthasan, V. Murugesan, *J. Electron Spectrosc. Relat. Phenom.*, **2019**, *231*, 2.

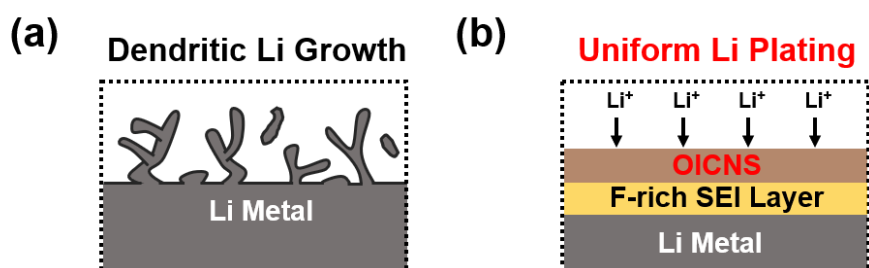


Figure 3.1. Schematic illustrations of Li deposition on Li metal anodes with different separators. (a) Dendritic Li growth is ceaselessly propagated when the poly(propylene) (PP) separator is solely adopted on the Li metal. (b) Uniform Li ion deposition is effectively achieved by using the **OICNS** between the PP separator and Li metal.

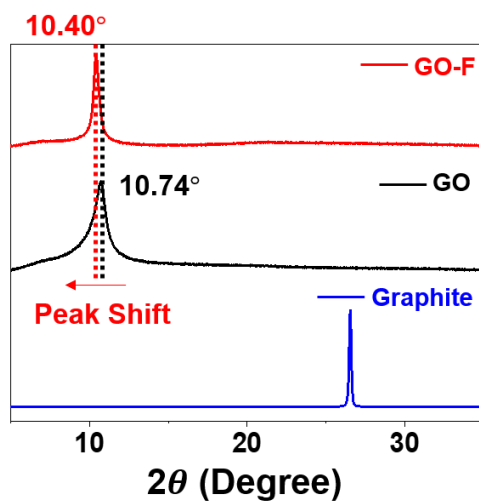


Figure 3.2. XRD results of GO-F, GO, and graphite.

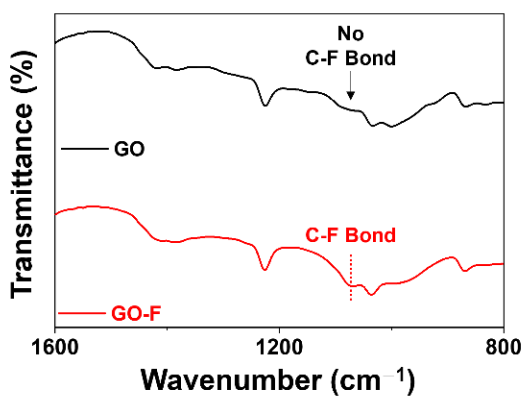


Figure 3.3. FT-IR spectra of GO and GO-F.

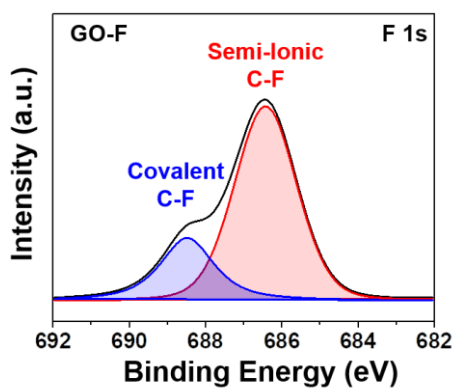


Figure 3.4. F 1s XPS spectra of **GO-F**.

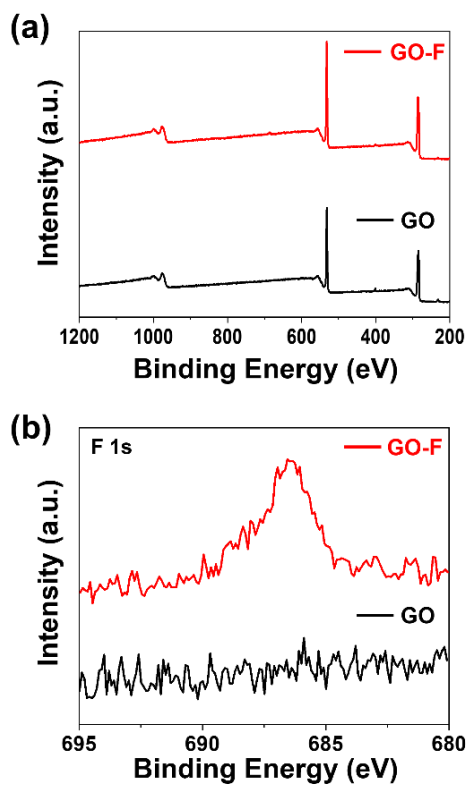


Figure 3.5. (a) XPS profile of GO and **GO-F**. (b) High resolution F 1s XPS profile of GO and **GO-F**.

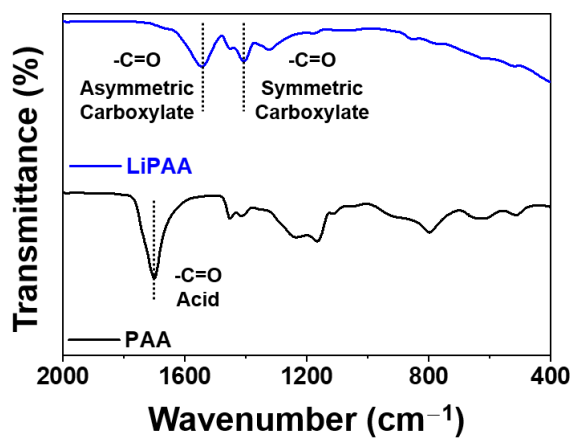


Figure 3.6. FT-IR spectra of PAA and LiPAA.

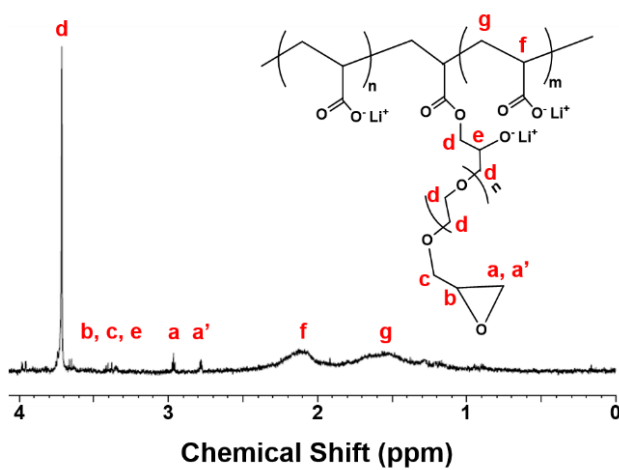


Figure 3.7. ^1H NMR spectrum of PAA-PEGDGE (D_2O , 400 MHz).

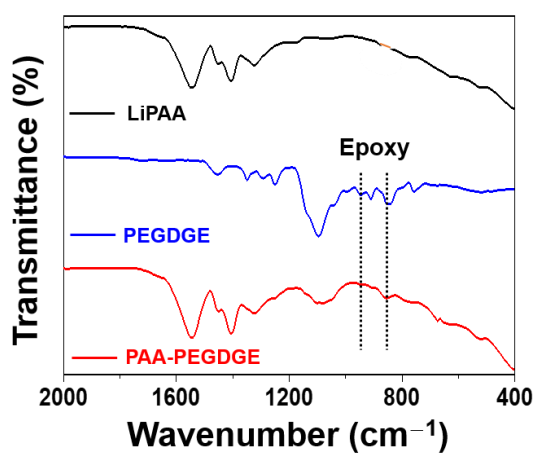


Figure 3.8. FT-IR profiles of LiPAA, PEGDGE, and **PAA-PEGDGE**.

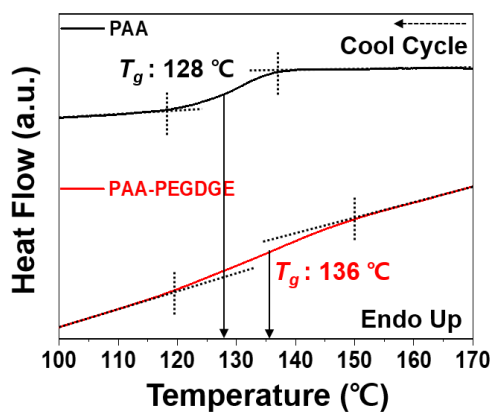


Figure 3.9. DSC profiles of PAA and **PAA-PEGDGE**.

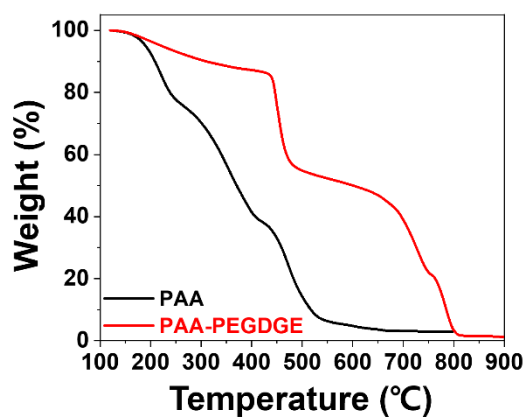


Figure 3.10. TGA curves of PAA and PAA-PEGDGE.

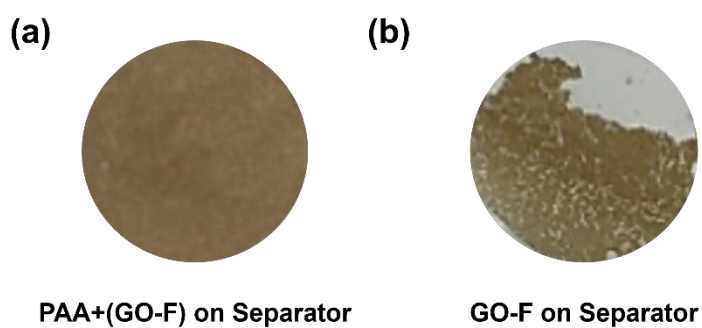


Figure 3.11. Photographs of (a) PAA+GO-F mixture and (b) the GO-F particles on the PP separator.

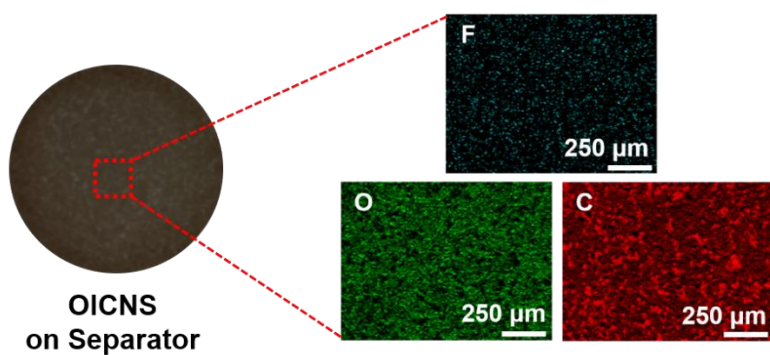


Figure 3.12. Photograph and SEM-EDS elemental mapping of the **OICNS**.

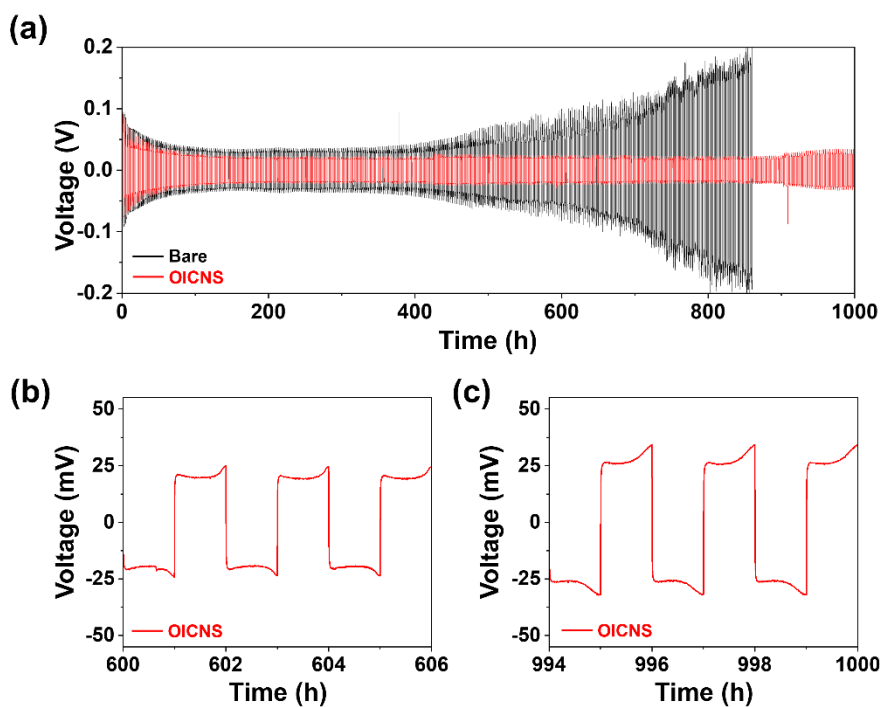


Figure 3.13. (a) Electrochemical performances of Li symmetric cells with the PP separator and the **OICNS** at 1 mA cm^{-2} with a capacity of 1 mAh cm^{-2} . The magnified voltage-time curves of Li symmetric cell with the **OICNS** at 1 mA cm^{-2} with a capacity of 1 mAh cm^{-2} (b) from 600 h to 606 h and (c) from 994 h to 1000 h.

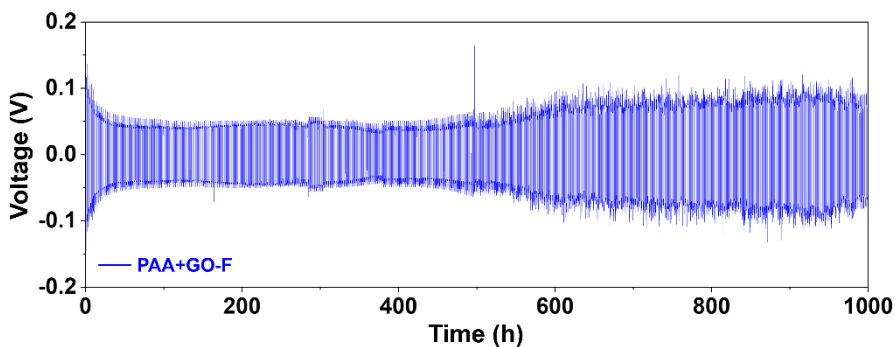


Figure 3.14. Electrochemical performances of Li symmetric cell with PAA+GO-F layer at 1 mA cm^{-2} with a capacity of 1 mAh cm^{-2} .

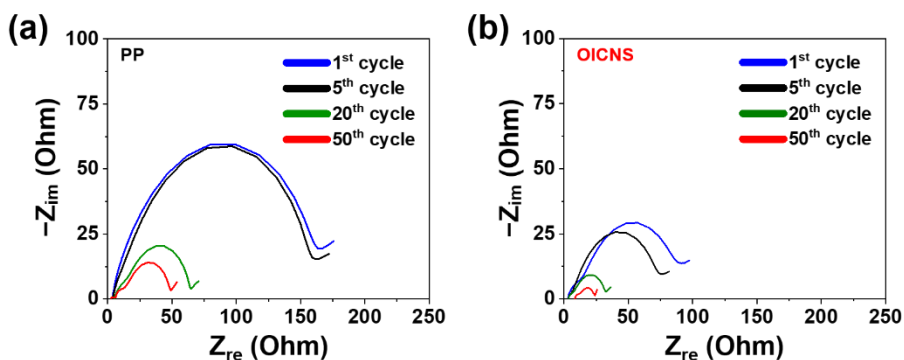


Figure 3.15. The EIS spectra of Li symmetric cells with (a) the PP separator and (b) the **OICNS** after 1st, 5th, 20th, and 50th cycle.

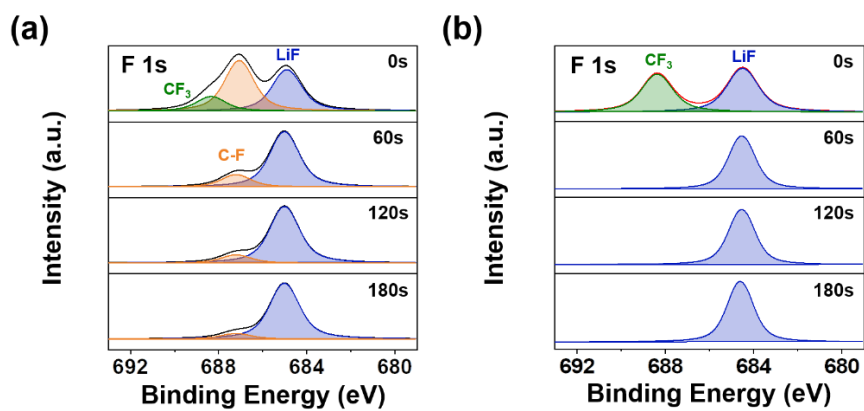


Figure 3.16. F 1s XPS depth profiles of Li metal anodes after 5 cycles for (a) the PP separator and (b) the OICNS.

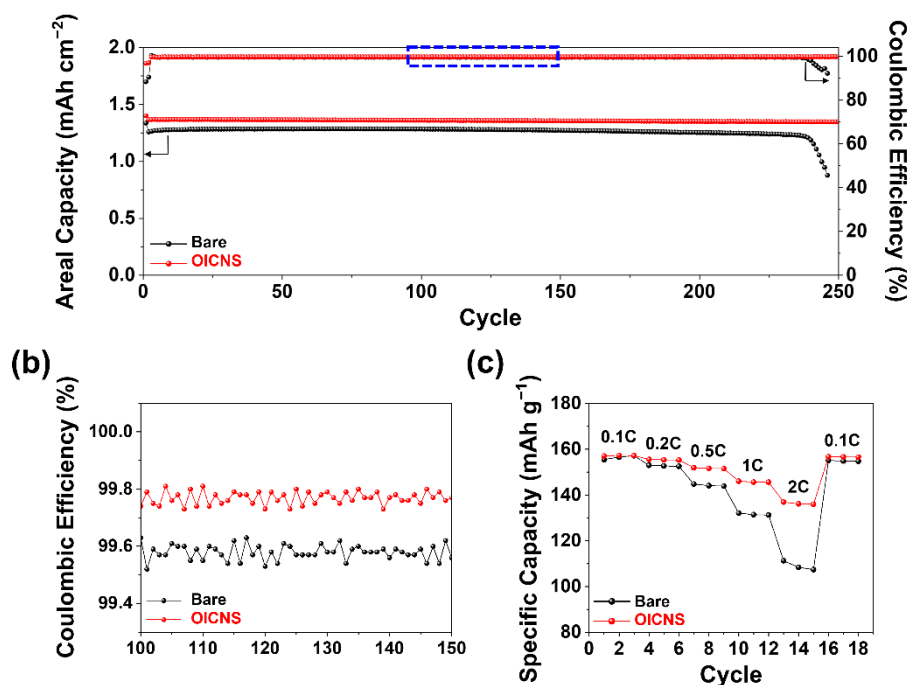


Figure 3.17. Electrochemical performance of LFP-Li full-cells with the PP separator and the **OICNS**. Cycling performance of the full cells at 0.5C when the mass loading of LFP is (a) 10.0 mg cm^{-2} and (b) their coulombic efficiencies. (c) Rate performance of LFP-Li full cells containing the PP separator and the **OICNS**.

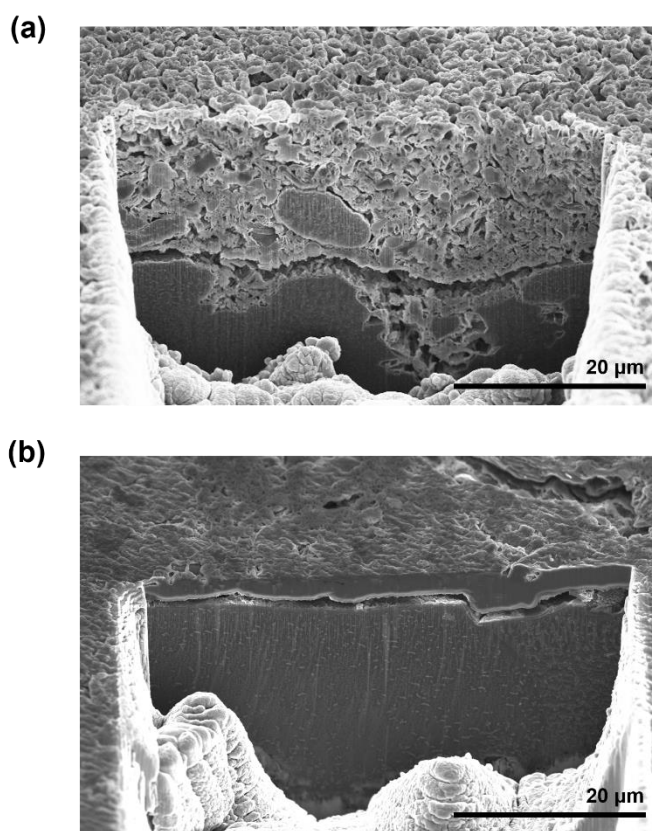


Figure 3.18. Cross-sectional SEM images of Li metal electrodes after 20th discharge with (a) the PP separator and (b) the **OICNS**.

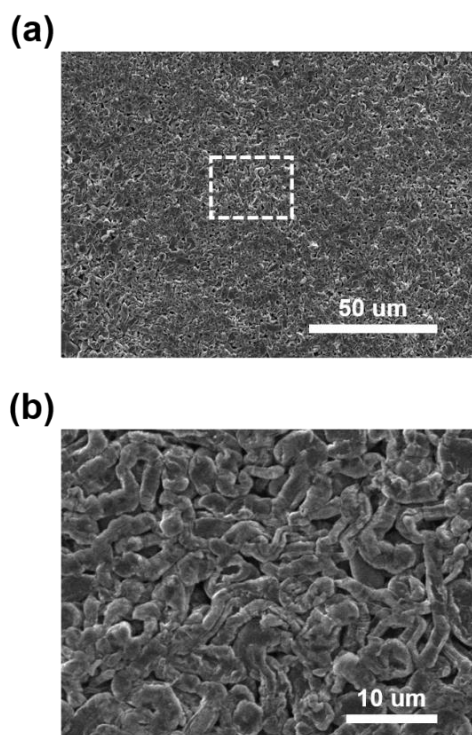


Figure 3.19. (a) SEM images of Li metal electrodes after 20th cycling in Li symmetric cells with the PP separator and (b) magnification of the area enclosed by the white box.

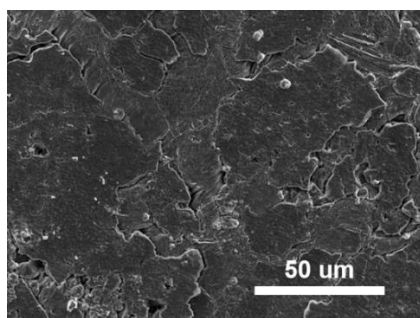


Figure 3.20. SEM images of Li metal electrodes after 20th cycling in Li symmetric cells with the OICNS.

국문 초록

리튬 이온 배터리의 등장은 전기차의 상용화를 통해 우리 삶에 큰 변화를 가져왔다. 전기차 개발이 활발히 진행되고 보편화되고 있지만, 고속 충전 및 장거리 주행 문제를 극복하기 위한 방안은 여전히 고민해야 할 과제이다. 따라서 배터리의 내부 저항을 낮추고 에너지 밀도를 높일 수 있는 소재를 사용하는 것의 필요성이 존재한다. 음극 활물질은 전해질과의 계면이 불안정하고 반복적인 충/방전 과정에서 그 구조가 변하기 때문에 이러한 음극의 문제를 해결하는 것은 매우 중요하다. 다양한 전략 중 고분자를 음극에 도입하는 것은 적은 양으로도 뚜렷한 효과를 낼 수 있어 많은 주목을 받고 있다. 이와 같은 맥락에서, 우리는 흑연, 실리콘 및 리튬 금속 등 각각의 음극재에 대한 최적의 고분자 디자인을 제안하여 결과적으로 계면 안정성을 유지하고 전기화학적 성능을 향상시켰다.

1장에서는 계면 저항을 낮추고 고속에서의 구동 능력을 향상시키기 위해 흑연 음극 용 스타디엔-부타디엔 고무/카르복시메틸 셀룰로오스 바인더 체계에 글리세롤을 첨가제로 도입하였다. 글리세롤은 가소제 역할을 수행하여 고분자 사슬 간 결정성을 낮추고 높은 유전 특성으로 균일한 전하 분포를 유도하여 음극 계면에서 리튬 이온 확산을 촉진한다. 결과적으로, 소량의 글리세롤을 첨가하면 고속 성능이 향상된다. 이 연구는 전극 및 슬러리의 주요 특성을 희생하지 않으면서 리튬 이온 배터리의 성능 향상과 관련된 매개변수를 개선하기 위한 바인더 첨가제로서의 단분자의 유용성을 강조한다.

2장에서는 금속 이온-유기화합물 배위 결합에 의한 동적 가교 및 전극 제조 과정의 열처리에 의한 인 시추 가교를 포함하는 실리콘/탄소 계 전극 용 바인더를 보고한다. 금속 이온-유기화합물 배위 결합의 가역성과 에틸렌 글라이콜의 유연성은 바인더 네트워크의 우수한 탄성에 종합적으로 기여한다. 해당 바인더 네트워크는 입자를 결합하고 전극 구조를 안정시켜, 장기적인 수명 특성을 높인다. 또한, 바인더를 상용 수준의 면적 용량에 적용했을 때 안정적인 사이클 특성을 구현할 수 있었다. 이 연구는 고용량 합금 기반 전극을 위한 내의 금속 이온-유기화합물 배위 화학의 중요성을 강조한다.

3장에서는 리튬 메탈 계면 안정화를 위해 유기 성분으로는 폴리 아크릴산 기반의 고분자, 무기 성분으로는 불소화 그래핀 옥사이드를 합성 후 가교하여 두 성분이 시너지 효과를 내는 보호막을 보고한다. 두 물질의 가교로 더 견고한 보호막 네트워크를 개발할 수 있었다. 불소화 그래핀 옥사이드의 높은 기계적 강도와 폴리 아크릴산의 점탄성은 수지상 리튬 성장 없이 안정된 계면을 유지한다. 특히 불소화 그래핀 옥사이드의 불소 작용기는 불소화 리튬 성분이 풍부한 내부 고체-전해질 계면을 유도하여 초기부터 안정된 전기화학 성능을 구현하는 데에 기여한다. 본 연구는 유/무기 보호막을 활용하여 리튬 금속 음극 계면의 물리적, 화학적 특성을 변화시키는 것이 안정된 계면 유지에 기여한다는 것을 강조한다.

주요어 : 리튬 이온 배터리, 리튬 메탈 배터리, 바인더 첨가제, 고분자 바인더, 보호막, 계면 안정성

학 번 : 2019-21638

List of publications

International Peer-Reviewed Journals (First Author)

1. J. Kim, **K. Park**, Y. Cho, H. Shin, S. Kim, K. Char, and J. W. Choi, “Zn²⁺–Imidazole Coordination Crosslinks for Elastic Polymeric Binders in High-Capacity Silicon Electrodes” *Advanced Science*, **2021**, 8, 2004290 (*IF*=17.521).
2. **K. Park**, S. Kim, J. Kim, G. Seo, M. Baek, Y. Cho, J. Lee, J. W. Choi, “Glycerol as a Binder Additive for Low Resistance Graphite Anodes in Lithium Ion Batteries (100th birthday of Prof. John B. Goodenough Article)” *Journal of The Electrochemical Society* (*IF*=4.386).

International Peer-Reviewed Journals (Co-author)

1. Y. Cho, J. Kim, A. Elabd, S. Choi, **K. Park**, T.-w. Kwon, J. Lee, K. Char, A. Coskun, and J. W. Choi, “A Pyrene–Poly (acrylic acid)–Polyrotaxane Supramolecular Binder Network for High-Performance Silicon Negative Electrodes” *Advanced Materials*, **2019**, 31, 1905048 (IF=32.086).
2. S. Yasmeen, M. R. Khan, **K. Park**, Y. Cho, J. W. Choi, H.-S. Moon* “Preparation of a Hydrophobic Cerium Oxide Nanoparticle Coating with Polymer Binder via a Facile Solution Route” *Ceramics International*, **2020**, 46, 8, 12209-12215 (IF=5.160).
3. S. Ryu, T. Sugimoto, J. Kim, **K. Park**, D. Im, Y.-G. Lee, and J. W. Choi, “Synergistic Composite Coating for Separators in Lithium Metal Batteries” *ACS Applied Energy Materials*, **2021**, 4, 5237-5245 (IF=6.959).
4. C. H. Moon, S. Yasmeen, **K. Park**, H. Gaiji, C. Chung, H. Kim, H.-S Moon, J. W. Choi, H-B-R Lee* “Icephobic Coating through a Self-formed Superhydrophobic Surface Using a Polymer and Microsized Particles” *ACS Applied Mater. & Interfaces*, **2022**, 14, 2, 3334-3343 (IF=10.383).
5. J. Kim, J. Choi, **K. Park**, S. Kim, K. W. Nam, K. Char, and J. W. Choi, “Host-Guest Interlocked Complex Binder for Silicon-Graphite Composite Electrodes in Lithium Ion Batteries” *Advanced Energy Materials*, **2022**, 12, 11, 2103718 (IF=29.698).
6. J. Kim, M. Baek, **K. Park**, Y. Park, I. Hwang, J. W. Choi* “Effect of Ionotropic Gelation of COOH-Functionalized Polymeric Binders in Multivalent Ion Batteries” *J. Solid State Electrochem.*, **2022**, 26, 1969 (IF=2.747).

Patents

1. 최장욱, 박기호, 김재민, 이정민, 조윤식 “리튬 이차 전지용 음극 및 이를 포함하는 리튬 이차 전지”, (특허 출원 10-2021-0188684, 2021.12.27)
2. 최장욱, 김재민, 박기호, 이정민 “리튬이차전지용 전극 바인더 및 이를 포함하는 전극과 리튬이차전지”, (특허 출원 10-2021-0104198, 2021.08.06)